THE JOURNAL OF BIOLOGICAL CHEMISTRY VOL. 291, NO. 4, pp. 1538–1551, January 22, 2016

Hajdu Cheney Mouse Mutants Exhibit Osteopenia, Increased Osteoclastogenesis, and Bone Resorption*◆

Received for publication, August 14, 2015, and in revised form, November 18, 2015 Published, JBC Papers in Press, December 1, 2015, DOI 10.1074/jbc.M115.685453

Ernesto Canalis[‡§1], **Lauren Schilling**[‡], **Siu-Pok Yee**[¶‖], **Sun-Kyeong Lee**[§**], **and Stefano Zanotti**[‡§]

From the Departments of [‡]*Orthopaedic Surgery,* [§]*Medicine,* [¶]*Cell Biology, Genetics, and* [‖]*Genome Sciences Biology, **Center on Aging, University of Connecticut Health Center, Farmington, Connecticut 06030*

Notch receptors are determinants of cell fate and function and play a central role in skeletal development and bone remodeling. Hajdu Cheney syndrome, a disease characterized by osteoporosis and fractures, is associated with *NOTCH2* mutations resulting in a truncated stable protein and gain-of-function. We created a mouse model reproducing the Hajdu Cheney syndrome by introducing a 6955C→T mutation in the *Notch2* locus leading to a Q2319X change at the amino acid level. *Notch2*^{Q2319X} heterozygous mutants were smaller and had shorter femurs than controls; and at 1 month of age they exhibited cancellous and cortical bone osteopenia. As the mice matured, cancellous bone volume was restored partially in male but not female mice, whereas cortical osteopenia persisted in both sexes. Cancellous bone histomorphometry revealed an increased number of osteoclasts and bone resorption, without a decrease in osteoblast number or bone formation. Osteoblast differentiation and function were not affected in *Notch2*^{Q2319X} cells. The pre-osteoclast cell pool, osteoclast differentiation, and bone resorption in response to receptor activator of nuclear factor κB ligand *in vitro* were increased in *Notch2*^{Q2319X} mutants. These effects were suppressed by the γ-secretase inhibitor LY450139. In conclusion, *Notch2*^{Q2319X} mice exhibit cancellous and cortical bone osteopenia, enhanced osteoclastogenesis, and increased bone resorption.

Notch proteins are four single-pass transmembrane receptors that play a critical role in cell fate decisions (Fig. 1) (1–4). Notch regulates cell renewal and plays a role in skeletal development and homeostasis and in osteoblast and osteoclast differentiation (4–8). Jagged1 and -2 and DeltaLike1, -3, and -4 are the five classic Notch ligands (4). Notch-ligand interactions result in the proteolytic cleavage and release of the Notch intracellular domain (NICD),[2] which translocates to the nucleus to form a complex with recombination signal-binding protein for immunoglobulin κJ region (Rbpjκ) and Mastermind-like to regulate transcription (9–12). This canonical signaling pathway leads to the transcription of Hairy Enhancer of Split (Hes)1, -5, and -7 and Hes related with YRPW motif (Hey)1, -2, and -L.

Skeletal cells express Notch1, Notch2, and low levels of Notch3 transcripts (13–15). Activation of Notch in undifferentiated and differentiated osteoblasts inhibits cell differentiation and function and causes osteopenia (16, 17). In contrast, activation of Notch1 in osteocytes causes a pronounced increase in bone mass due to a suppression of bone resorption (18). Results from the conditional inactivation of *Notch1* and *Notch2* in the developing skeleton confirmed the inhibitory role of Notch in osteoblastogenesis (6, 19). Whereas substantial work has characterized the consequences of Notch1 gain-of-function in the skeleton, there is limited knowledge on the function of Notch2 in the postnatal skeleton. This knowledge is particularly important because Notch1 and Notch2 do not have redundant functions, and Notch1 inhibits, whereas Notch 2 enhances, osteoclastogenesis (13, 20–24).

Hajdu Cheney syndrome is a devastating disease characterized by focal bone lysis of distal phalanges and by generalized osteoporosis (25, 26). Hajdu Cheney syndrome is transmitted as an autosomal dominant disease, although sporadic cases occur. Whole exome sequencing in families affected by Hajdu Cheney syndrome revealed the presence of point mutations or short deletions in exon 34 of *NOTCH2* leading to the creation of a stop codon and the premature termination of the protein product upstream from the PEST (proline (P), glutamic acid (E), serine (S), and (T) threonine) domain (27–31). Because the PEST domain is necessary for the ubiquitinylation and degradation of Notch, the mutations lead to a stable NICD protein and persistence of NOTCH2 signaling because the sequences required for the formation of the Notch transcriptional complex are preserved (Fig. 1). Despite the pronounced skeletal abnormalities reported in Hajdu Cheney syndrome, little is known regarding the mechanisms underlying the bone loss or the effects of Notch2 gain-of-function in the skeleton. Information obtained from iliac crest bone biopsies has been inconclusive and reported in a small number of subjects with Hajdu Cheney syndrome (32–35).

The purpose of this work was to gain understanding on the Hajdu Cheney syndrome skeletal phenotype and the mechanisms involved. To this end, we created a mouse model reproducing the *NOTCH2* mutation (6949C→T) found in a subject affected by the disease and presenting with pronounced osteoporosis and fractures (28, 30). To create a Hajdu Cheney syn-

* This work was supported by grant DK045227 from the National Institute of Diabetes and Digestive and Kidney Diseases. The authors declare that they have no conflicts of interest with the contents of this article. The content is solely the responsibility of the authors and does not necessarily represent the official views of the National Institutes of Health.

◆ This article was selected as a Paper of the Week.

[1] To whom correspondence should be addressed: Depts. of Orthopaedic Surgery and Medicine, University of Connecticut Health Center, Farmington, CT 06030-5456. Tel.: 860-679-7978; Fax: 860-679-1474; E-mail: canalis@uchc.edu.

[2] The abbreviations used are: NICD, Notch intracellular domain; Alpl, alkaline phosphatase; αMEM, α-minimum essential medium; μCT, microcomputed tomography; neo, neomycin; NF, nuclear factor; qRT-PCR, quantitative reverse transcription-PCR; Rankl, receptor activator of NF-κB ligand; Rbpjκ, recombination signal binding protein for immunoglobulin κJ region; TRAP, tartrate resistant acid phosphatase.

drome mutant mouse, we introduced the human *NOTCH2* mutation of 6949C→T into the corresponding base of the mouse *Notch2* (6955C→T) gene, creating a stop codon in exon 34 and leading to a Q2319X change at the amino acid level with a truncated Notch2 protein of 2318 amino acids (Fig. 1). In this study, we define the skeletal phenotype of *Notch2*^{Q2319X} mutant mice and the mechanisms responsible.

Experimental Procedures

Hajdu Cheney Mutant Mice—To create a mouse model of Hajdu Cheney syndrome, we reproduced the mutation reported in a subject with the disease (28, 30). In the individual, a C at nucleotide 6949 from the translational start of *NOTCH2* mutated into a T (6949C→T) leading to the creation of a premature stop codon in exon 34. The mutation corresponding to the 6949C→T substitution (6955C→T) was introduced into the mouse *Notch2* locus by homologous recombination. A targeting vector containing 4.6 kb of 5′-homology arm from exon 30 to exon 33 of *Notch2*, a phosphoglycerate kinase promoter-driven neomycin (neo) selection cassette flanked by *loxP* sites ~400 nucleotides upstream of exon 34, a 6955C→T mutation, and a 3′-homology arm of 3.0 kb, was used (Fig. 1). Embryonic (ES) cells from 129Sv/C57BL/6j embryos were electroporated, and G418-resistant colonies were selected. Targeted clones were verified by long range polymerase chain reaction (PCR) of genomic DNA. To ensure proper integration of the 5′-homology arm, we used forward F1 5′-GGTTGACAGGTGATGCAGTGCCAG-3′ and reverse R1 5′-GGCTGGACGTAAACTCCTCTTCAG-3′ primers followed by nested forward F2 5′-GCACATACCACACGGTCAGCTGAG-3′ and reverse R2 5′-GATCGGAATTGGGCTGCAGGAATT-3′ primers. To ensure proper integration of the 3′-homology arm, forward F3 5′-GGCTTCTGAGGCGGAAAGAACCAG-3′ and reverse R3 5′-CAATGGGGAGCCGTCATCATCGG-3′ primers were used (Fig. 1*B*). The presence of the 6955C→T mutation in the selected clone was confirmed by DNA sequencing (GENEWIZ, South Plainfield, NJ) (Fig. 1). Targeted ES clones were used for aggregations to generate chimeric mice at the Gene Targeting and Transgenic Facility of University of Connecticut Health Center. Chimeric male mice were bred with female mice expressing Cre under the control of the hypoxanthine-guanine phosphoribosyltransferase (*Hprt*) promoter to remove the *PGKneo* cassette (36). The removal of the cassette was verified by PCR, and the *Hprt-Cre* transgene was segregated by crossing with C57BL/6j wild type mice. Genomic DNA was obtained from ear punches of F1 pups, and the *Notch2* mutation was confirmed by DNA sequencing (GENEWIZ) as shown in Fig. 1*C*. Genotyping of *Notch2*^{Q2319X} mice was conducted in tail DNA extracts by PCR using forward primer *Nch2Lox* gtF 5′-CCCTTCTCTCTGTGCGGTAG-3′ and reverse primer *Nch2Lox* gtR 5′-CTCAGAGCCAAAGCCTCACTG-3′. In this study, we characterized 129Sv/C57BL/6j mutant mice and sex-matched littermate controls obtained by crossing heterozygous *Notch2*^{Q2319X} Hajdu Cheney mutants with wild type mice. Studies were approved by the Institutional Animal and Care Use Committees of Saint Francis Hospital and Medical Center and University of Connecticut Health Center.

Microcomputed Tomography (μCT)—Bone microarchitecture of femurs from experimental and control mice was determined using a microcomputed tomography instrument (μCT 40; Scanco Medical AG, Bassersdorf, Switzerland), which was calibrated periodically using a phantom provided by the manufacturer (37, 38). Femurs were scanned in 70% ethanol at high resolution, energy level of 55 peak kV, intensity of 145 μA, and integration time of 200 ms. A total of 100 slices at midshaft and 160 slices at the distal metaphysis were acquired at an isotropic voxel size of 216 μm^3 and a slice thickness of 6 μm and were chosen for analysis. Trabecular bone volume fraction and microarchitecture were evaluated starting ~1.0 mm proximal from the femoral condyles. Contours were manually drawn every 10 slices a few voxels away from the endocortical boundary to define the region of interest for analysis. The remaining slice contours were iterated automatically. Trabecular regions were assessed for total volume, bone volume, bone volume fraction (bone volume/total volume), trabecular thickness, trabecular number, trabecular separation, connectivity density, and structure model index, using a Gaussian filter ($\sigma = 0.8$) and user-defined thresholds (37, 38). For analysis of femoral cortical bone, contours were iterated across 100 slices along the cortical shell of the femoral midshaft, excluding the marrow cavity. Analysis of bone volume/total volume, porosity, cortical thickness, total cross-sectional and cortical bone area, periosteal perimeter, endosteal perimeter, and material density was performed using a Gaussian filter ($\sigma = 0.8$, support = 1), and user defined thresholds.

Bone Histomorphometric Analysis—Static and dynamic cancellous bone histomorphometry was carried out on experimental and control mice after they were injected with calcein, 20 mg/kg, and demeclocycline, 50 mg/kg, at an interval of 2 days in 1-month-old or of 5 days in 3-month-old animals. Five micron longitudinal sections of undecalcified femurs embedded in methyl methacrylate were cut on a microtome (Microm, Richards-Allan Scientific, Kalamazoo, MI) and stained with 0.1% toluidine blue or von Kossa. Static parameters of bone formation and resorption were measured in a defined area between 360 and 2160 μm from the growth plate, using an OsteoMeasure morphometry system (Osteometrics, Atlanta, GA). For dynamic histomorphometry, mineralizing surface per bone surface and mineral apposition rate were measured on unstained sections under ultraviolet light, using a triple diamidino-2-phenylindole/fluorescein/Texas red set long pass filter, and bone formation rate was calculated.

For cortical histomorphometry, femurs from 1- and 3-month-old mice were embedded in methyl methacrylate and cut through the mid-diaphysis with an EXAKT Precision Saw. Slides were ground using an EXAKT 400 CS micro grinding system to a thickness of ~15 μm and surface-polished. Cortical sections were processed either in-house or at Alizee Pathology (Baltimore, MD). Slides were left unstained for fluorescence microscopy or stained with hematoxylin/eosin to establish cellular parameters and analyzed at a magnification of ×400 using OsteoMeasureXP software. Stained sections were used to draw the cortical bone, marrow space, osteoid, and cell surfaces as well as to count osteocytes within the cortex and osteoblasts and osteoclasts along the endocortical surface. Data from

1-month-old mice were generated from an all-inclusive cortical section, whereas data from 3-month-old mice were obtained from approximately half of a cortical section. Osteocyte number was expressed as cells/bone area measured. The terminology and units used for cancellous and cortical bone are those recommended by the Histomorphometry Nomenclature Committee of the American Society for Bone and Mineral Research (39, 40).

Biochemical Parameters of Bone Turnover—Serum levels of C-terminal collagen cross-links, procollagen type 1 N-terminal propeptide, and tartrate-resistant acid phosphatase form 5b (TRACP5b) were measured by enzyme-linked immunosorbent assay (ELISA) (Immunodiagnostic Systems, Bolton, England). Serum from *Notch2*^{Q2319X} and control littermate mice was obtained following an overnight fast, and assays were conducted according to the manufacturer's instructions.

Osteoblast-enriched Cell Cultures—The parietal bones of 3–5-day-old control and *Notch2*^{Q2319X} mutant mice were exposed to type II collagenase from *Clostridium histolyticum* (Worthington) pretreated with *N*-α-tosyl-L-lysyl-chloromethyl ketone hydrochloride at 17 μg/ml (Calbiochem) (41). Bones were digested for 20 min at 37 °C; cells were extracted in five consecutive reactions, and cells from the last three digestions were pooled and seeded at a density of 10,000 cells/cm^2, as described (42). Osteoblast-enriched cells were cultured in Dulbecco's modified Eagle's medium (DMEM) supplemented with non-essential amino acids (both from Gibco and Life Technologies, Inc.), 20 mM HEPES, 100 μg/ml ascorbic acid (both from Sigma), and 10% heat-inactivated fetal bovine serum (FBS; Atlanta Biologicals, Norcross, GA) in a humidified 5% CO_2 incubator at 37 °C. To promote maturation, confluent osteoblasts were exposed to DMEM supplemented with 10% heat-inactivated FBS, 100 μg/ml ascorbic acid, and 5 mM β-glycerophosphate (Sigma).

Transient Transfections—Osteoblast-enriched cells were transfected with a plasmid containing six dimeric CSL or Rbpjκ consensus sequences upstream of the β-globin basal promoter (12×CSL-Luc; L. J. Strobl, Munich, Germany) or with 2.9- and 2.0-kb fragments of the *Hey1* (Hey1-Luc; M. M. Maier, Wuerzburg, Germany) or *Hey2* (Hey2-Luc; T. Iso, Los Angeles, CA) promoter and cloned upstream of luciferase (43–45). Transfections were conducted in cells cultured to 70% confluence using X-tremeGENE 9 (1.5 μl of X-tremeGENE 9:1 μg of DNA), according to manufacturer's instructions (Roche Applied Science). A construct where the cytomegalovirus (CMV) promoter directs the expression of β-galactosidase (CMV/β-galactosidase; Clontech) was used to correct for transfection efficiency. Cells were exposed to the X-tremeGENE 9/DNA mix for 16 h, and the medium was replaced after 24 h. Subsequently, cells were harvested in reporter lysis buffer (Promega, Madison, WI) and lysed by freezing at −80 °C and thawing at 37 °C. Luciferase and β-galactosidase activities were determined, respectively, with the luciferase assay system kit (Promega) and galacton plus (Life Technologies, Inc.) in accordance with manufacturer's instructions on an Optocomp luminometer (MGM Instruments, Hamden, CT).

Osteocyte-enriched Cultures—Osteocyte-enriched cells were obtained following a modification of a previously described method (46). Femurs were removed aseptically from 1-month-old experimental and control mice; the surrounding tissues were dissected; the proximal epiphyseal end was excised, and the bone marrow was removed by centrifugation. The distal epiphysis was excised, and femurs were digested for 20 min at 37 °C with type II bacterial collagenase pretreated with *N*-α-tosyl-L-lysyl-chloromethyl ketone hydrochloride and subsequently exposed to 5 mM EDTA for 20 min at 37 °C. The resulting osteocyte-enriched cortical femurs were cultured individually in DMEM supplemented with nonessential amino acids (both from Life Technologies, Inc.), 100 μg/ml ascorbic acid, and 10% FBS for 3 days at 37 °C in a humidified 5% CO_2 incubator. Cells were cultured in the absence or presence of the γ-secretase inhibitor LY450139 (Selleck Chemicals, Houston, TX), dissolved in dimethyl sulfoxide (DMSO), and tested at 1 μM (47). An equal amount of DMSO was added to control cultures.

Bone Marrow Cell Cultures and Osteoclast Formation—Bone marrow cells were isolated from the femurs by a modification of previously published methods (48, 49). Briefly, bone marrow cells were collected by centrifugation and washed twice with α-minimum essential medium (MEM) (Life Technologies, Inc.) and cultured overnight in α-MEM containing 10% FBS. Nonadherent cells were collected, and bone marrow mononuclear cells were isolated using Ficoll-Hypaque (GE Healthcare) density gradient centrifugation. The interface between Ficoll-Hypaque and medium was collected, and cells were seeded at a density of 1×10^6 cells/cm^2 and cultured in α-MEM with 10% heat-inactivated FBS (GE Healthcare) in the presence of macrophage colony-stimulating factor (M-Csf) at 30 ng/ml and receptor activator of nuclear factor κB ligand (Rankl) at 1–30 ng/ml (both from R&D Systems, Minneapolis, MN) for 6 days. In a subsequent experiment, total bone marrow cells were isolated from femurs by centrifugation, cultured in α-MEM in the presence of M-Csf at 100 ng/ml for 6 days, and switched to α-MEM containing M-Csf at 30 ng/ml and Rankl at 10–30 ng/ml for 8 days. Cells were cultured in the absence or presence of the γ-secretase inhibitor LY450139 at 1 μM or DMSO (47). In both experiments, cultured medium was changed every 3 days and cells were fixed for 30 s at room temperature prior to tartrate-resistant acid phosphatase (TRAP) enzyme histochemistry using a commercial kit (Sigma), in accordance with the manufacturer's instructions. TRAP-positive cells that contained more than three nuclei were considered osteoclast-like cells.

In Vitro Bone Resorption Assay—Bone marrow cells were isolated from femurs by centrifugation, expanded in the presence of M-Csf at 100 ng/ml for 5 days, and seeded at a density of 30,000 cells/cm^2 on bovine cortical bone slices in α-MEM with 10% FBS and M-Csf at 30 ng/ml and Rankl at 30 ng/ml each for 16 days. Culture medium was replaced every 4 days with fresh medium containing M-Csf and Rankl. To visualize resorption pits, bone slices were sonicated to remove osteoclasts and stained with 1% toluidine blue in 1% sodium borate. To evaluate the ability of osteoclasts to resorb bone, the number of individual pits and resorption area were measured on images acquired with an Olympus DP72 camera using CellSens Dimension software version 1.6 (Olympus Corp., Center Valley, PA) (50).

TABLE 1
Primers used for qRT-PCR determinations
GenBank™ accession numbers identify transcript recognized by primer pairs.

Gene	Strand	Sequence 5′–3′	GenBank™ accession no.
Acp5	Forward	GACAAGAGGTTCCAGGAGAC	NM_001102404; NM_001102405; NM_007388
	Reverse	TTCCAGCCAGCACATACC	
Alpl	Forward	TGGTATGGGCGTCTCCACAGTAACC	NM_007431; NM_001287172; NM_001287176
	Reverse	CTTGGAGAGGGCCACAAAGG	
Bglap	Forward	GACTCCGGCGCTACCTTGGGTAAG	NM_001037939
	Reverse	CCCAGCACAACTCCTCCCTA	
Casp3	Forward	ATGGAGAACAACAAAACCTC	NM_009810; NM_001284409
	Reverse	CCATGTATGGTCTTTACTTCA	
Gapdh	Forward	CCCCTCTGGAAAGCTGTGGCGT	NM_008084; NM_001289726
	Reverse	AGCTTCCCGTTCAGCTCTGG	
Hes1	Forward	ACCAAAGACGGCCTCTGAGCACAGAAAGT	NM_008235
	Reverse	ATTCTTGCCCTTCGCCTCTT	
Hey1	Forward	ATCTCAACAACTACGCATCCCAGC	NM_010423
	Reverse	GTGTGGGTGATGTCCGAAGG	
Hey2	Forward	AGCGAGAACAATTACCCTGGGCAC	NM_013904
	Reverse	GGTAGTTGTCGGTGAATTGGACCT	
HeyL	Forward	CAGTAGCCTTTCTGAATTGCGAC	NM_013905
	Reverse	AGCTTGGAGGAGCCCTGTTTC	
Nfatc1	Forward	GCGCAAGTACAGTCTCAATGGCC	NM_198429; NM_001164110; NM_001164111; NM_001164112; NM_00116641091; NM_016791
	Reverse	GGATGGTGTGGGTGAGTGGT	
Notch2	Forward	CATCGTGACTTTCCA	NM_010928
	Reverse	GGATCTGGTACATAGAG	
Rpl38	Forward	AGAACAAGGATAATGTGAAGTTCAAGGTTC	NM_001048057; NM_001048058; NM_023372
	Reverse	CTGCTTCAGCTTCTCTGCCTTT	
Tnfrsf11b	Forward	CAGAAAGGAAATGCAACACATGACAAC	NM_008764
	Reverse	GCCTCTTCACACAGGGTGACATC	
Tnfsf11	Forward	TATAGAATCCTGAGACTCCATGAAAAC	NM_011613
	Reverse	CCCTGAAAGGCTTGTTTCATCC	

Flow Cytometry—Bone marrow cells were obtained by flushing tibiae and collecting cells in α-MEM. After washing in α-MEM, the red blood cells were lysed with ammonium chloride/potassium lysis buffer (Life Technologies, Inc.), and the cell preparation was filtered through a nylon mesh and counted. Dead cells were excluded by their ability to incorporate propidium iodide. Anti-mouse antibodies used for flow cytometric analysis were anti-CD45R (B220) for B-cell lineage cells, anti-CD3 for T-cell lineage cells, anti-CD11b (Mac-1) for macrophage lineage cells, anti-CD117 (c-Kit), a hematopoietic stem cell marker, and anti-CD115 (c-Fms, the M-Csf receptor) (all from BD Biosciences). Antibodies conjugated to fluorochromes, or biotinylated, and secondary step reagents were obtained commercially (eBioscience, San Diego, CA). Labeling of bone marrow cells for flow cytometric analysis was performed by standard staining procedures in Hanks' balanced salt solution (Life Technologies, Inc.) containing 0.01 M HEPES (pH 7.4), supplemented with 2% FBS. Flow cytometric analysis was carried out on a FACSCalibur instrument and data analysis performed using FlowJo software (Tree Star Inc., Ashland, OR) (51).

Quantitative Reverse Transcription (qRT)-PCR—Total RNA was extracted from cells or femurs, following the removal of the bone marrow by centrifugation, and mRNA levels determined by qRT-PCR (52, 53). For this purpose, equal amounts of RNA were reverse-transcribed using iScript RT-PCR kit (Bio-Rad), according to manufacturer's instructions, and amplified in the presence of specific primers (Table 1, all primers from Integrated DNA Technologies (IDT), Coralville, IA), and iQ SYBR Green Supermix (Bio-Rad), at 60 °C for 35 cycles. Transcript copy number was estimated by comparison with a serial dilution of cDNA for acid phosphatase 5, tartrate-resistant (*Acp5*, from Thermo Scientific, Pittsburgh, PA), alkaline phosphatase (*Alpl*, from American Type Tissue Culture Collection, ATCC, Manassas, VA), bone γ-carboxyglutamate protein (*Bglap*, encoding for osteocalcin, from J. Lian, Burlington, VT), caspase 3 (*Casp3*) (from GE Healthcare), *Hes1* (from ATCC), *Hey1* and *Hey2* (both from T. Iso), *HeyL* (from D. Srivastava, Dallas, TX), nuclear factor of activated T cells 1 (*Nfatc1*, from A. Rao, La Jolla, CA), tumor necrosis factor receptor superfamily 11b (*Tnfrsf11b*, encoding for osteoprotegerin, from ATCC), or tumor necrosis factor, member 11 (*Tnfsf11*, encoding for Rankl, from Source BioScience, Nottingham, UK) (54–58).

To measure levels of the $Notch2^{6955C\rightarrow T}$ mutant transcript, total RNA was reverse-transcribed with Moloney murine leukemia virus reverse transcriptase, in accordance with the manufacturer's instructions (Life Technologies, Inc.), in the presence of reverse primers for *Notch2* and of reverse primers for either ribosomal protein L38 (*Rpl38*) or glyceraldehyde-3-phosphate dehydrogenase (Gapdh) (Table 1). *Notch2* cDNA was amplified by qPCR in the presence of specific primers (Table 1), a TET-labeled DNA probe of sequence 5′-CATTGC-CTAGGCAGC-3′ covalently bound to a 3′-minor groove binder quencher (Life Technologies, Inc.), and SsoAdvanced Universal Probes Supermix (Bio-Rad) at 60 °C for 45 cycles (59). *Rpl38* or *Gapdh* cDNA was amplified as described above. $Notch2^{6955C\rightarrow T}$ transcript copy number was estimated by comparison with a serial dilution of a synthetic DNA fragment (IDT) containing ~200 bp surrounding the 6955C→T mutation in the *Notch2* locus and cloned into pcDNA3.1(−) (Life Technologies, Inc.) by isothermal single reaction assembly using commercially available reagents (New England Biolabs, Ipswich, MA) (60).

Amplification reactions were conducted in a CFX96 qRT-PCR detection system (Bio-Rad), and fluorescence was moni-

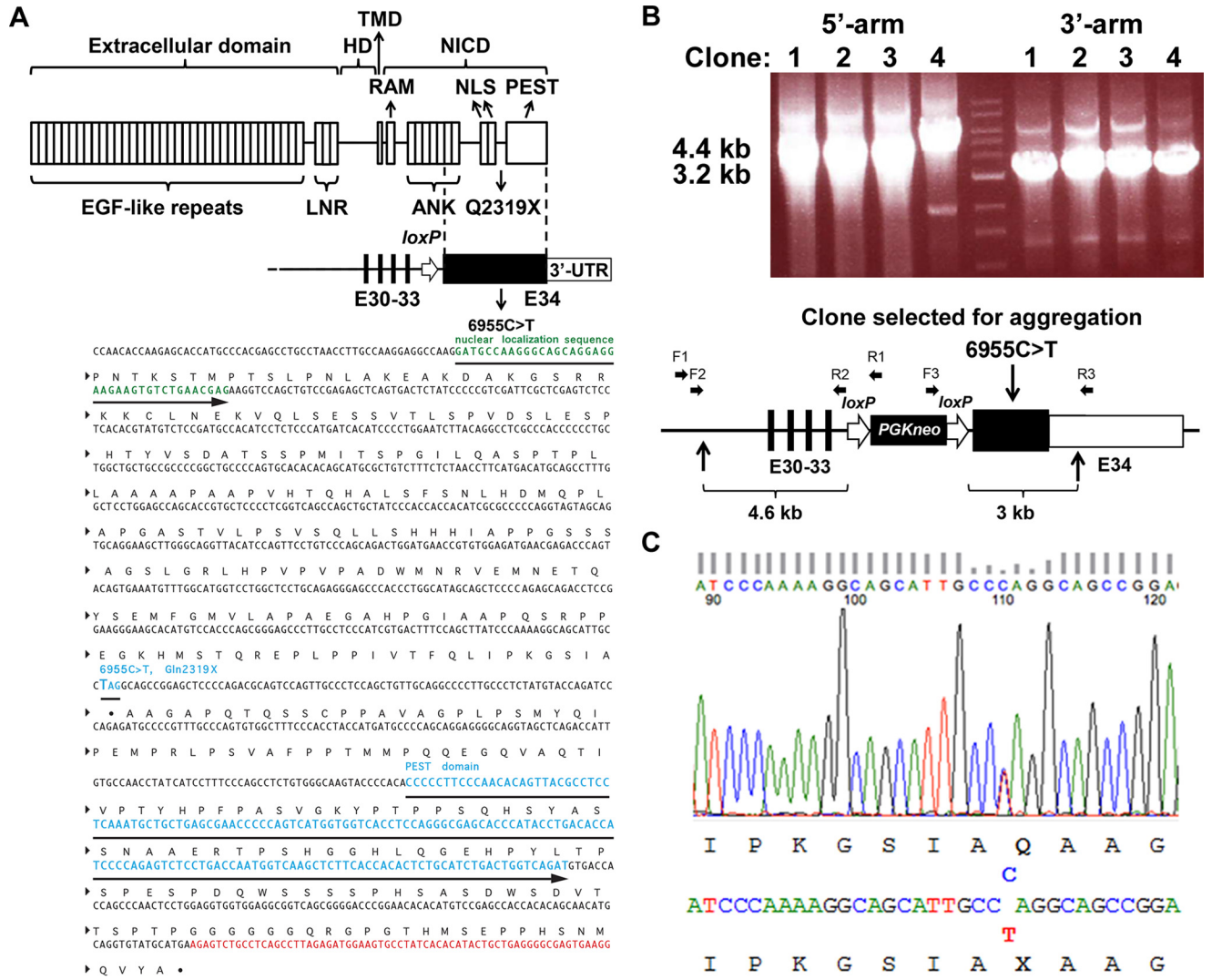

FIGURE 1. **Domains of Notch2 and engineering of the Hajdu Cheney *Notch2*^{Q2319X} mutant allele.** *A, upper panel* shows domains of the Notch2 receptor depicting the following: 1) extracellular domain containing multiple epidermal growth factor (*EGF*)-like tandem repeats upstream of Lin12-Notch repeats (*LNR*); 2) heterodimerization domain (*HD*) which, in association with the LNR, forms the negative regulatory region; 3) transmembrane domain (*TMD*); and 4) Notch intracellular domain (*NICD*) consisting of an Rbpjκ-association module (*RAM*) linked to ankyrin (*ANK*) repeats and a nuclear localization sequence (*NLS*), upstream from a PEST domain. Under the Notch2 protein domains, the genomic structure of mutant exon 34 aligned with the corresponding protein structure. *Black bars* represent exons (*E*) 30–33, *black box* exon 34 containing the 6955C→T mutation leading to a Notch2^{Q2319X} truncated protein, and *white box* the 3′-untranslated region (UTR). Position of the *loxP* site remaining following the excision of the neo selection cassette is indicated by the *white arrow*. *Lower panel A* shows the region of the *Notch2* locus surrounding the 6955C→T substitution; DNA coding for the nuclear localization sequence (*green*), the PEST domain (*blue*), and the *Notch2* 3′-UTR (*red*). *B,* identification of four targeted ES clones by long range PCR. Correct targeting of the 5′- and 3′- homology arms into the *Notch2* locus was documented by the presence of a 4.4- (*left*) and 3.2-kb (*right*) PCR product in each of four clones. The *middle lane* represents molecular weight markers. Clone 2 was selected for ES cell aggregation. The *lower panel* in *B* shows the structure of the linearized targeting vector, consisting of a 4.6-kb 5′-homology arm containing exons 30–33 of *Notch2*, followed by a phosphoglycerate kinase promoter-driven neo selection cassette flanked by *loxP* sites ~400 nucleotides upstream of exon 34. *Vertical arrows* on the bottom indicate the boundaries of the linearized targeting vector. *Black boxes* indicate coding sequences, and *white box* indicates the 3′-UTR. *Horizontal arrows* indicate binding sites for the primers used for the long range PCR. Primer pairs *F1-R1* and *F2-R2* were used for amplification of the 5′-homology arm, and primer pairs *F3-R3* were used for amplification of the 3′-homology arm. *C,* genomic DNA from ear samples of F1 pups was used as a template for PCR, and products were sequenced by the Sanger method. The 1:1 signal ratio of C (*blue*) to T (*red*) demonstrates the presence of the 6955C→T substitution and heterozygosity of the mutation.

tored during every PCR cycle at the annealing step. Data are expressed as copy number corrected for *Rpl38* or *Gapdh* copy number, estimated by comparison with a serial dilution of *Rpl38* (from ATCC) or *Gapdh* (from R. Wu, Ithaca, NY), respectively (61, 62). To establish changes in gene expression in osteoblast-enriched cultures, data were obtained from three experiments and controls normalized to 1.

Statistics—Data are expressed as means ± S.D. Statistical differences were determined by unpaired Student's *t* test or analysis of variance with Holm-Sidak post hoc analysis for pairwise or multiple comparisons.

Results

Generation and General Appearance of Hajdu Cheney Notch2^{Q2319X} *Mutant Mice*—To introduce a Hajdu Cheney syndrome mutation into the *Notch2* locus, a targeting vector containing a 6955C→T substitution in exon 34 (Fig. 1) was introduced into ES cells derived from an F1 129Sv/C57LB/6j

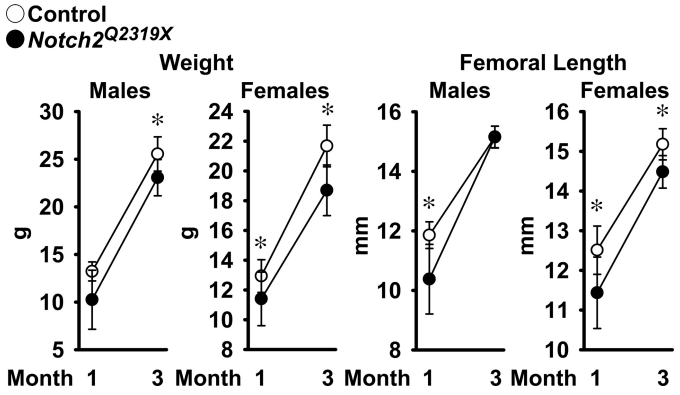

FIGURE 2. **Weight and femoral length of male and female Hajdu Cheney *Notch2*^{Q2319X} mutant mice (*filled circles*) and littermate wild type controls (*open circles*).** Values are means ± S.D. The number of observations is as follows: male control mice $n = 5$ at 1 month and $n = 9$ at 3 months; female control mice $n = 9$ at 1 month and $n = 4$ at 3 months; male *Notch2*^{Q2319X} $n = 6$ at 1 month and $n = 10$ at 3 months; and female *Notch2*^{Q2319X} $n = 8$ at 1 month and $n = 7$ at 3 months of age. *, significantly different between *Notch2*^{Q2319X} mutant mice and control, $p < 0.05$ by unpaired *t* test.

embryo by electroporation. A targeted clone was used to generate mutant mice, which were studied following the removal of the selection cassette. Breedings between heterozygous Hajdu Cheney *Notch2*^{Q2319X} mutant mice resulted in perinatal lethality, whereas matings of heterozygous mutants with wild type mice resulted in no apparent lethality and a similar distribution of 56% wild type and 44% mutant mice in the offspring. Therefore, heterozygous Hajdu Cheney mutant mice were compared with wild type littermates following heterozygous crossings with wild type mice, all in a 129Sv/C57BL/6j genetic background. At 1 month of age, *Notch2*^{Q2319X} heterozygous mice weighed ~20% less than littermate controls, but their general appearance was not substantially different from controls. As the mice matured, there was less difference in the size of mutant and wild type mice, and mutant mice weighed ~10% less than wild types at 3 months of age. Femoral length was 12% shorter in *Notch2*^{Q2319X} heterozygous mice of both sexes than controls at 1 month of age, but at 3 months of age, femoral length in *Notch2*^{Q2319X} mice was not different from controls in male mice and was only 5% shorter in female mice (Fig. 2).

Femoral Microarchitecture and Histomorphometry of Hajdu Cheney Mutant Mice—μCT of the distal femur revealed that male *Notch2*^{Q2319X} mutant mice had a 50% decrease in trabecular bone volume at 1 month of age, whereas female mice had a 20% decrease in trabecular bone volume (Table 2 and Fig. 3). The osteopenia was due to a reduction in the number of trabeculae and to a lesser extent to a decrease in trabecular thickness. The decreased cancellous bone volume in male mice was associated with decreased connectivity. The decrease in trabecular number was sustained and observed in 3-month-old *Notch2*^{Q2319X} mutant mice resulting in a non-significant decrease in cancellous bone volume of 30% in male mice and a significant decrease of 50% in female mice (Table 2). There were pronounced changes in the cortical bone structure of *Notch2*^{Q2319X} mutants of both sexes; cortical bone was thin and porous, and total area as well as bone area were reduced (Table 2 and Fig. 3). The decrease in cortical bone and overall bone size was more pronounced in *Notch2*^{Q2319X} at 1 month of age,

TABLE 2

Femoral microarchitecture assessed by μCT of 1- and 3-month-old *Notch2*^{Q2319X} mutant mice and littermate controls

μCT was performed in distal femurs for trabecular bone and midshaft for cortical bone from 1- and 3-month-old male and female *Notch2*^{Q2319X} mutant mice and control littermates (Control). Values are means ± SD.

Males	1 Month		3 Month	
	Control n = 5	*Notch2*^{Q2319X} n = 6	Control n = 9	*Notch2*^{Q2319X} n = 10
Distal Femur Trabecular Bone				
Bone Volume/Total Volume (%)	9.1 ± 2.9	4.2 ± 1.5*	7.7 ± 3.4	5.4 ± 2.5
Trabecular Separation (μm)	160 ± 15	250 ± 28*	208 ± 19	278 ± 36*
Trabecular Number (1/mm)	6.3 ± 0.6	4.1 ± 0.5*	4.8 ± 0.4	3.7 ± 0.5*
Trabecular Thickness (μm)	24 ± 3	20 ± 2*	33 ± 5	33 ± 5
Connectivity Density (1/mm^3)	600 ± 233	186 ± 154*	197 ± 82	124 ± 67*
Structure Model Index	2.6 ± 0.4	3.0 ± 0.3	2.6 ± 0.4	2.7 ± 0.3
Density of Material (mg HA/cm^3)	875 ± 10	870 ± 63	976 ± 19	957 ± 12*
Femoral Midshaft Cortical Bone				
Bone Volume/Total Volume (%)	80.5 ± 1.1	70.7 ± 5.6*	90.0 ± 0.8	87.5 ± 1.4*
Porosity (%)	19.6 ± 1.1	29.3 ± 5.6*	10.0 ± 0.8	12.5 ± 1.4*
Cortical Thickness (μm)	82 ± 7	55 ± 10*	155 ± 11	128 ± 9*
Total Area (mm^2)	1.5 ± 0.1	1.2 ± 0.2*	1.8 ± 0.1	1.7 ± 0.2
Bone Area (mm^2)	0.46 ± 0.04	0.32 ± 0.07*	0.77 ± 0.05	0.65 ± 0.07*
Periosteal Perimeter (μm)	4.4 ± 0.1	3.9 ± 0.4*	4.7 ± 0.1	4.6 ± 0.2
Endocortical Perimeter (mm)	3.7 ± 0.1	3.4 ± 0.3	3.6 ± 0.1	3.6 ± 0.2
Density of Material (mg HA/cm^3)	960 ± 20	926 ± 44	1167 ± 13	1122 ± 12*

Females	1 Month		3 Month	
	Control n = 9	*Notch2*^{Q2319X} n = 8	Control n = 4	*Notch2*^{Q2319X} n = 7
Distal Femur Trabecular Bone				
Bone Volume/Total Volume (%)	7.2 ± 1.2	5.7 ± 1.1*	3.6 ± 1.4	1.8 ± 0.8*
Trabecular Separation (μm)	189 ± 19	243 ± 25*	296 ± 40	376 ± 50*
Trabecular Number (1/mm)	5.4 ± 0.5	4.2 ± 0.5*	3.4 ± 0.5	2.7 ± 0.4*
Trabecular Thickness (μm)	24 ± 2	22 ± 1	34 ± 3	26 ± 2*
Connectivity Density (1/mm^3)	461 ± 102	400 ± 173	67 ± 43	32 ± 28
Structure Model Index	2.7 ± 0.2	2.7 ± 0.2	3.1 ± 0.3	3.0 ± 0.3
Density of Material (mg HA/cm^3)	887 ± 15	875 ± 10	1002 ± 6	978 ± 18*
Femoral Midshaft Cortical Bone				
Bone Volume/Total Volume (%)	85.6 ± 1.5	81.2 ± 2.8*	90.4 ± 1.1	88.6 ± 1.0*
Porosity (%)	14.4 ± 1.5	18.8 ± 2.8*	9.6 ± 1.1	11.4 ± 1.0*
Cortical Thickness (μm)	95 ± 9	75 ± 9*	147 ± 25	130 ± 6
Total Area (mm^2)	1.6 ± 0.1	1.4 ± 0.1*	1.7 ± 0.1	1.4 ± 0.1*
Bone Area (mm^2)	0.49 ± 0.05	0.39 ± 0.05*	0.77 ± 0.07	0.59 ± 0.02*
Periosteal Perimeter (μm)	4.5 ± 0.2	4.2 ± 0.2	4.6 ± 0.2	4.3 ± 0.1*
Endocortical Perimeter (mm)	3.7 ± 0.2	3.5 ± 0.2	3.4 ± 0.1	3.3 ± 0.1
Density of Material (mg HA/cm^3)	993 ± 27	966 ± 38	1164 ± 12	1110 ± 9*

* Significantly different from controls, $p < 0.05$ by unpaired *t*-test.

although cortical bone architecture remained affected at 3 months of age in *Notch2*^{Q2319X} mutants of both sexes.

Cancellous bone histomorphometric analysis of femurs from *Notch2*^{Q2319X} mutant mice at 1 month of age confirmed the microarchitectural findings and demonstrated decreased bone volume/tissue volume secondary to a decrease in trabecular number in male and female mutant mice (Table 3 and Fig. 3). At 1 month of age, there was an increase in osteoclast surface/bone surface and eroded surface in *Notch2*^{Q2319X} mutant mice, and there was no change in osteoblast number/perimeter, osteoblast surface, bone formation rate, or osteocyte number/bone area. This indicates that enhanced bone resorption without a coupled bone-forming response was responsible for the skeletal phenotype. At 3 months of age, the cellular phenotype evolved. The numbers of osteoclasts and eroded surface were no longer significantly increased, and osteoblast surface and mineral apposition rates were increased in male mice, a possible reflection of increased bone remodeling or a compensatory bone-forming response to the enhanced bone resorption noted at 1 month of age. An increase in osteoblast number and mineralizing surface was not observed in female mice. Although trabecular number was decreased by ~30% in 3-month-old male mice, bone volume/total volume was only modestly affected,

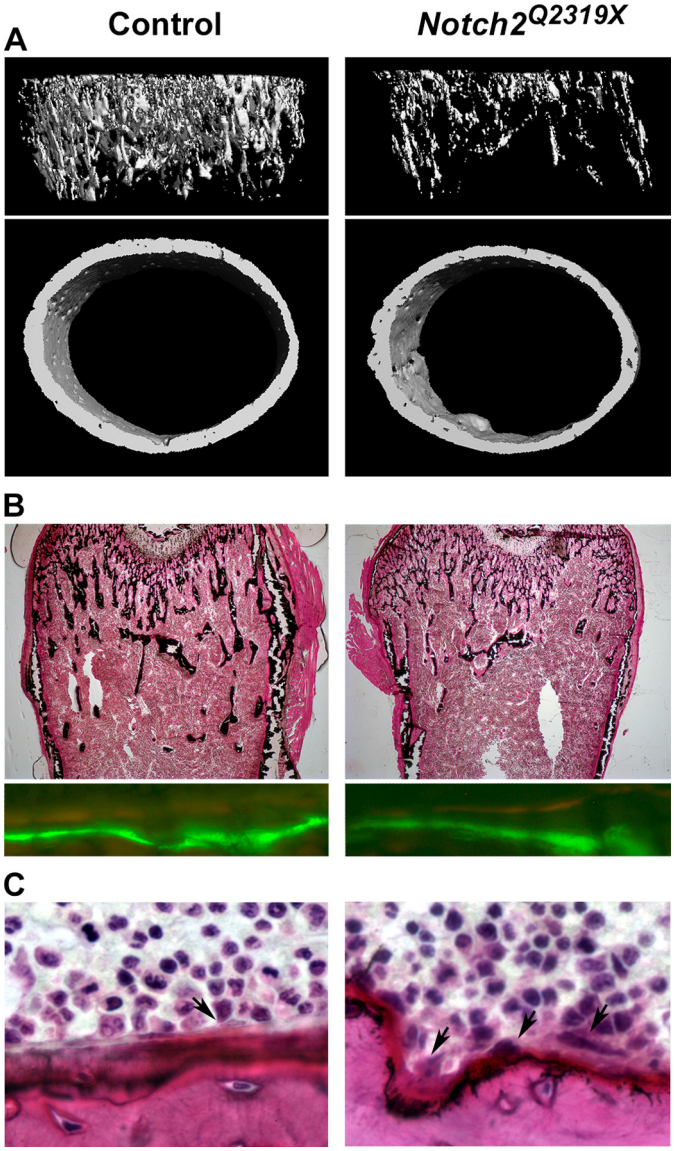

FIGURE 3. *A*, representative microcomputed tomography images of proximal trabecular bone and midshaft of femurs, showing cancellous bone osteopenia and decreased trabecular number and thinner and porous cortical bone in male *Notch2*^{Q2319X} mutant mice. Complete data set is shown in Table 2. *B*, representative static cancellous bone histological sections stained with toluidine blue show decreased number of trabeculae in Hajdu Cheney *Notch2*^{Q2319X} mice and calcein and demeclocycline labels show no differences in mineral apposition rate between control and *Notch2*^{Q2319X} mice. Complete data set is in Table 3. *C*, cross-sectional cortical bone stained with hematoxylin and eosin. *Arrows* in *C* point to osteoclasts on the endocortical surface. Complete data set is in Table 4. All representative images are from femurs from 1-month-old male Hajdu Cheney *Notch2*^{Q2319X} mutant and littermate wild type controls.

TABLE 3

Cancellous bone histomorphometry of 1- and 3-month-old *Notch2*^{Q2319X} mutant mice and littermate controls

Bone histomorphometry was performed in distal femurs from 1- and 3-month old male and female *Notch2*^{Q2319X} mutant mice and control littermates (Control). Values are means ± SD.

Males	1 Month		3 Month	
	Control n = 5	*Notch2*^{Q2319X} n = 6	Control n = 7	*Notch2*^{Q2319X} n = 8
Distal Femur Trabecular Bone				
Bone Volume/Tissue Volume (%)	9.2 ± 1.7	4.5 ± 2.9*	8.9 ± 2.0	6.9 ± 1.9^{+}
Trabecular Separation (μm)	267 ± 22	779 ± 611*	325 ± 67	461 ± 63*
Trabecular Number (1/mm)	3.4 ± 0.2	1.8 ± 1.2*	2.9 ± 0.6	2.0 ± 0.2*
Trabecular Thickness (μm)	27 ± 5	24 ± 6	30 ± 3	33 ± 7
Osteoblast Surface/Bone Surface (%)	22 ± 4	23 ± 5	12 ± 4	22 ± 7*
Osteoblasts/Bone Perimeter (1/mm)	25.3 ± 4.5	27.7 ± 7.3	14.1 ± 3.9	23.1 ± 6.3*
Osteoid Surface/Bone Surface (%)	4.6 ± 3.4	3.3 ± 1.1	1.7 ± 1.2	3.4 ± 2.7
Osteoclast Surface/Bone Surface (%)	10.5 ± 1.1	13.5 ± 1.8*	5.8 ± 1.9	7.7 ± 2.0
Osteoclasts/Bone Perimeter (1/mm)	7.2 ± 0.8	9.5 ± 1.6*	4.2 ± 1.5	5.5 ± 1.3
Eroded Surface/Bone Surface (%)	19.1 ± 2.5	25.5 ± 3.6*	10.3 ± 3.9	13.2 ± 3.7
Osteocytes/Bone Area (mm^2)	539 ± 106	502 ± 96	542 ± 103	602 ± 66
	n = 3	n = 4	n = 5	n = 6
Mineral Apposition Rate (μm/day)	2.5 ± 0.1	2.4 ± 0.7	2.7 ± 0.2	3.8 ± 0.6*
Mineralizing Surface/Bone Surface (%)	12.0 ± 3.5	8.6 ± 1.5	13.2 ± 4.0	10.7 ± 1.9
Bone Formation Rate (μm^3/μm^2/day)	0.30 ± 0.09	0.20 ± 0.06	0.10 ± 0.05	0.15 ± 0.03

Females	1 Month		3 Month	
	Control n = 9	*Notch2*^{Q2319X} n = 6	Control n = 5	*Notch2*^{Q2319X} n = 5
Distal Femur Trabecular Bone				
Bone Volume/Tissue Volume (%)	10.1 ± 2.7	6.3 ± 1.6*	5.0 ± 3.1	3.8 ± 1.0
Trabecular Separation (μm)	288 ± 34	429 ± 108*	602 ± 262	636 ± 158
Trabecular Number (1/mm)	3.1 ± 0.3	2.3 ± 0.6*	1.8 ± 0.7	1.6 ± 0.4
Trabecular Thickness (μm)	32 ± 6	27 ± 3	26 ± 7	24 ± 3
Osteoblast Surface/Bone Surface (%)	24 ± 4	23 ± 7	23 ± 9	31 ± 11
Osteoblasts/Bone Perimeter (1/mm)	25.8 ± 5.1	24.2 ± 4.9	25.3 ± 10.5	33.6 ± 11.9
Osteoid Surface/Bone Surface (%)	4.0 ± 3.0	3.2 ± 1.9	6.5 ± 4.0	4.8 ± 3.5
Osteoclast Surface/Bone Surface (%)	12.4 ± 2.1	15.5 ± 2.3*	9.4 ± 1.2	10.5 ± 1.7
Osteoclasts/Bone Perimeter (1/mm)	7.8 ± 1.4	10.0 ± 0.9*	7.1 ± 0.9	7.8 ± 1.2
Eroded Surface/Bone Surface (%)	19.0 ± 4.8	23.9 ± 2.5*	16.8 ± 2.5	17.9 ± 2.4
Osteocytes/Bone Area (mm^2)	679 ± 90	605 ± 147	680 ± 163	706 ± 112
	n = 7	n = 5	n = 4	n = 4
Mineral Apposition Rate (μm/day)	1.3 ± 0.6	1.6 ± 0.9	4.7 ± 0.5	3.7 ± 0.4*
Mineralizing Surface/Bone Surface (%)	6.0 ± 2.0	6.0 ± 2.3	5.1 ± 3.0	4.6 ± 3.7
Bone Formation Rate (μm^3/μm^2/day)	0.18 ± 0.05	0.18 ± 0.06	0.08 ± 0.04	0.06 ± 0.05

* Significantly different from controls, $p < 0.05$ by unpaired *t*-test.
$^{+}$ $p < 0.08$.

possibly because, over time, bone formation compensated for the initial increase in bone resorption.

Cortical bone histomorphometry confirmed a decrease in cortical thickness and revealed no difference in osteocyte number (Table 4). There was an increase in endocortical osteoclast number and eroded surface in 1-month-old *Notch2*^{Q2319X} mutants, but the osteoblast number was not different from controls. At 3 months of age, osteoblast, osteoclast, and osteocyte number were not different between mutant and control mice. The identity of cells in the periosteal surface could not be determined with confidence. Mineral apposition rate was not determined in *Notch2*^{Q2319X} mutants because limited areas contained well defined double labels. This may suggest that bone formation was impaired in cortical bone.

Although cancellous and cortical bone histomorphometry revealed increased bone resorption in *Notch2*^{Q2319X} mutants, serum levels of the biochemical markers of C-terminal collagen cross-links and procollagen type 1 N-terminal propeptide were not different between *Notch2*^{Q2319X} mice and control littermates of both sexes at 1 and 3 months of age, and TRACP5b values were variable (data not shown). This may indicate that bone remodeling was not increased because a bone-forming response was delayed and observed by bone histomorphometry only in 3-month-old male mutant mice or may indicate limited sensitivity and variability of serum assays used to determine bone remodeling (63, 64).

Mechanisms Operational in Notch2^{Q2319X} *Mutant Mice*—To explore mechanisms that may explain the phenotype of *Notch2*^{Q2319X} mutant mice, RNA was extracted from femurs from mutant and control mice. qRT-PCR revealed expression of *Notch2*$^{6955C\rightarrow T}$ (*Notch2*^{Q2319X}) and moderately increased mRNA levels of Notch target genes *Hey1*, *Hey2,* and *HeyL*, but not *Hes1*, in femurs from mutant mice confirming activation of Notch signaling in skeletal tissue (Fig. 4). In accordance with

TABLE 4

Cortical histomorphometry of 1- and 3-month-old *Notch2*^{Q2319X} mutant male mice and littermate controls

Cortical bone histomorphometry was performed at mid-diaphysis in femurs from 1- and 3-month-old male *Notch2*^{Q2319X} mutant mice and control littermates (control). Data from 1-month-old mice were generated from analysis of an all-inclusive cortical section, and data from 3-month-old mice were obtained from analysis of an approximate half-cortical section so that bone volume/total volume and total bone area were not calculated but are provided by μCT in Table 2. Osteocyte number was counted in either full or hemi-sections and expressed as cells/bone area measured. Values are means ± S.D.

	1 Month		3 Months	
	Control $n = 6$	*Notch2*^{Q2319X} $n = 4$	Control $n = 4$	*Notch2*^{Q2319X} $n = 4$
Cortical bone				
Bone volume/tissue volume (%)	38.1 ± 7.5	29.7 ± 4.8		
Cortical thickness (μm)	206 ± 30	168 ± 11*	219 ± 70	157 ± 54
Bone area (mm^2)	0.54 ± 0.11	0.42 ± 0.06		
Osteocyte no./bone area (mm^2)	1531 ± 385	1405 ± 263	796 ± 227	763 ± 140
Endocortical surface				
Osteoblasts/bone perimeter (1/mm)	26.0 ± 9.5	20.1 ± 7.4	10.4 ± 4.2	6.8 ± 2.3
Osteoclasts/bone perimeter (1/mm)	3.7 ± 0.6	6.9 ± 0.8*	1.0 ± 0.1	1.0 ± 0.3
Osteoclast surface/bone surface (%)	5.5 ± 0.8	10.2 ± 1.4*	1.7 ± 0.5	1.7 ± 0.4
Eroded surface/bone surface (%)	8.9 ± 2.6	15.5 ± 1.4*	2.2 ± 0.6	2.2 ± 0.9

* Significantly different from controls, $p < 0.05$ by unpaired *t* test.

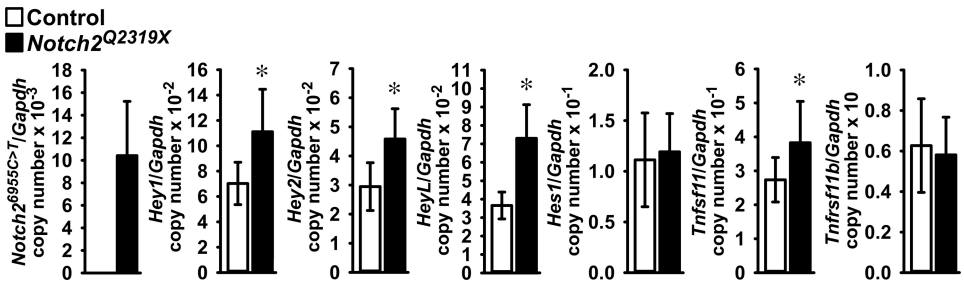

FIGURE 4. ***Notch*$^{6955C\rightarrow T}$ (*Notch2*^{Q2319X}), *Hey1*, *Hey2* and *HeyL*, *Hes1*, *Tnfsf11* (Rankl), and *Tnfrsf11b* (osteoprotegerin) mRNA levels in femoral bones from 1-month-old Hajdu Cheney *Notch2*^{Q2319X} mutant mice (*black bars*) and control littermate mice (*white bars*).** Transcript levels are expressed as copy number corrected for *Gapdh*. Values are means ± S.D.; $n = 8$ for control; $n = 9$ for *Notch2*^{Q2319X} for all transcripts. *, significantly different between *Notch2*^{Q2319X} mutants and control, $p < 0.05$ by unpaired *t* test.

the resorptive phenotype observed in 1-month-old mice, there was an increased expression of *Tnfsf11*, encoding for Rankl, in femurs from *Notch2*^{Q2319X} mutant mice, and no changes in *Tnfrsf11b*, encoding for osteoprotegerin.

Osteoblast-enriched and Osteocyte-enriched Cell Cultures—To understand the consequences of the Hajdu Cheney *Notch2*^{Q2319X} mutation in skeletal cells, osteoblast-enriched calvarial cells from mutant mice and littermate controls were cultured. Osteoblasts from *Notch2*^{Q2319X} mice expressed *Notch2*$^{6955C\rightarrow T}$ transcripts, which were not detected in wild type littermate controls. The expression of the Notch target genes *Hey1*, *Hey2,* and *HeyL* and the activity of the transiently transfected 12×CSL-Luc and Hey2-Luc (both $p < 0.05$) and Hey1-Luc ($p > 0.05$) reporter constructs were increased in *Notch2*^{Q2319X} osteoblasts confirming activation of Notch signaling (Fig. 5). In accordance with the histomorphometric findings revealing no changes in osteoblast number or function in 1-month-old *Notch2*^{Q2319X} mice, *Notch2*^{Q2319X} mutant cells expressed no significant changes in *Bglap* and *Alpl* mRNA levels (7, 17). In accordance with the increase in bone resorption observed in *Notch2*^{Q2319X} mice, expression of *Tnfsf11* was increased in osteoblast- (Fig. 5) and osteocyte-enriched preparations. This increase in osteocyte *Tnfsf11* was dependent on activation of Notch signaling because it was prevented by the addition of the γ-secretase inhibitor LY450139. *Tnfsf11/Rpl38* copy number was (means ± S.D.; $n = 4$ for all cultures) 1.2 ± 0.8 in control and 2.8 ± 0.7 ($p < 0.05$) in *Notch2*^{Q2319X} osteocyte-enriched cultures. In the presence of the LY450139, the values were 1.3 ± 0.6 in control and 1.1 ± 0.6 in *Notch2*^{Q2319X} cultures (not significant). In agreement with the lack of an effect of *Notch2*^{Q2319X} mutant on osteocyte number in cancellous and cortical bone, *Casp3* mRNA expression was not affected in osteocyte-rich cultures suggesting that osteocyte apoptosis was not enhanced in *Notch2*^{Q2319X} mutants. *Casp3/Rpl38* copy number was (means ± S.D.) 2.4 ± 1.6 ($n = 7$) in control and 2.4 ± 2.5 ($n = 9$) in *Notch2*^{Q2319X} cultures.

In Vitro Osteoclast Formation and Flow Cytometry—To investigate the cause of the increase in osteoclast number and bone resorption, the number of osteoclast precursors was determined in bone marrow cells from *Notch2*^{Q2319X} heterozygous and control littermates by flow cytometric analysis. There was a 25% increase in the fraction of B220$^-$ CD3$^-$ CD11b$^{-/lo}$, CD115 (c-Fms)^{high} CD117 (c-Kit)^{high} cells in *Notch2*^{Q2319X} mice compared with controls, and most of the early osteoclastogenic activity resides in these cells (50, 51). Further analysis of the monocyte/macrophage population present in the bone marrow B220$^-$ CD3$^-$ CD11b$^+$ CD115$^+$ fraction revealed no difference in additional osteoclast precursor cells between *Notch2*^{Q2319X} and control mice. Somatic *NOTCH2* gain-of-function mutations in exon 34 upstream from the PEST domain have been reported in B-cell lymphomas, and the B-cell fraction was analyzed by flow cytometry (65–67). There was no difference in the population of B-cells (B220$^+$ fraction) in the bone marrow from *Notch2*^{Q2319X} mice (means ± S.D.; $n = 4$), 34.8% ± 2.4, when compared with controls 31.9% ± 2.4.

To determine whether the *Notch2*^{Q2319X} mutation resulted in enhanced osteoclastogenesis, non-adherent bone marrow mononuclear cells isolated by Ficoll-Hypaque gradient centrif-

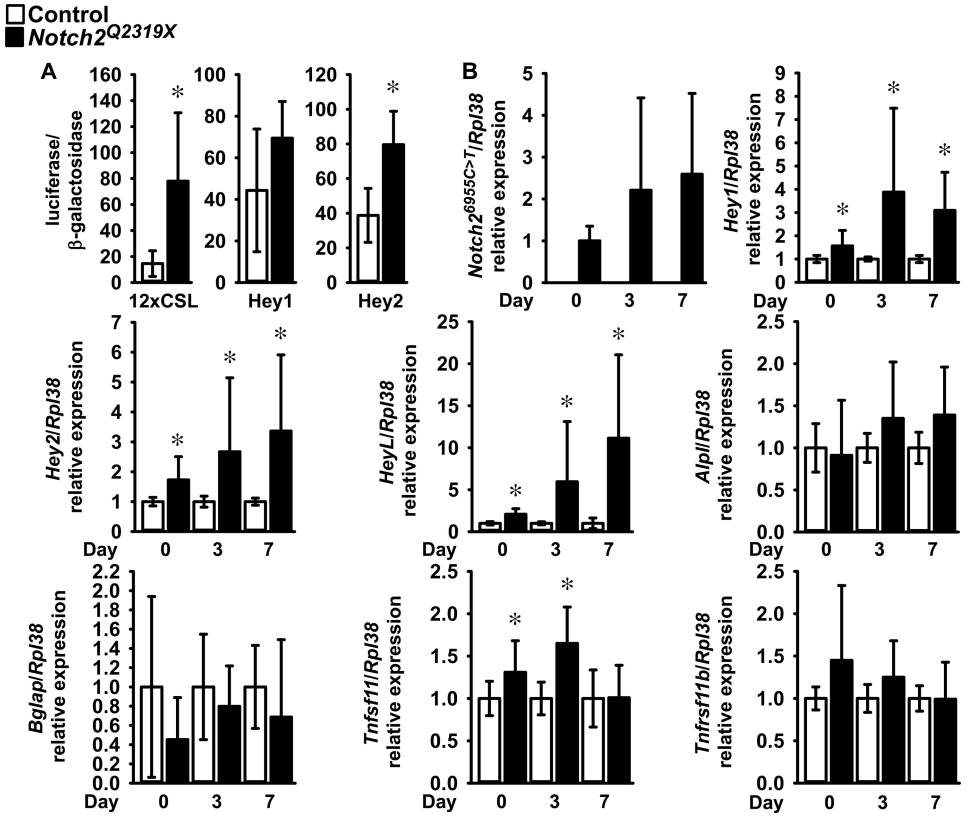

FIGURE 5. **Calvarial osteoblast-enriched cells from *Notch2*^{Q2319X} mutant (*black bars*) and wild type (*white bars*) littermate controls were isolated and cultured.** *A,* 12× CSL-Luc, Hey1-Luc, and Hey2-Luc reporter constructs were transiently co-transfected with a CMV β-galactosidase construct; data are expressed as luciferase/β-galactosidase activity. Values are means ± S.D.; $n = 6$ for all data sets. *B,* total RNA was extracted, and gene expression was measured by qRT-PCR in the presence of specific primers and probes. Data are expressed as *Notch2*$^{6955C\rightarrow T}$ (*Notch2*^{Q2319X}), *Hey1*, *Hey2*, *HeyL*, *Alpl*, *Bglap*, *Tnfsf11* (Rankl), and *Tnfrsf11b* (osteoprotegerin) copy numbers and corrected for *Rpl38*. Values are means ± S.D.; number of observations for control, $n = 12$ at 0 days, $n = 10$ at 3 days, and $n = 8$ at 7 days; number of observations for *Notch2*^{Q2319X}, $n = 12$ at 0 and at 3 days and $n = 8$ at 7 days for all transcripts. For mRNA expression, data were obtained from three experiments and controls normalized to 1. *, significantly different between *Notch2*^{Q2319X} mutant and wild type control cells, $p < 0.05$ by unpaired *t* test.

ugation were cultured in the presence of M-Csf at 30 ng/ml and Rankl at 1–30 ng/ml for 6 days and examined for the development of TRAP-positive multinucleated cells. There was a significant increase in the number of osteoclasts in bone marrow cell cultures from *Notch2*^{Q2319X} mutants compared with controls (Fig. 6). In accordance with the reported induction of *Nfatc1* by Notch2 in bone marrow macrophages, cells from *Notch2*^{Q2319X} expressed higher levels of *Nfatc1* mRNA than control cultures (20). Following treatment with Rankl at 30 ng/ml for 3 days, *Nfatc1/Rpl38* copy number was (means ± S.D.; $n = 4$) 5.1 ± 1.6 in control and 8.0 ± 1.6 ($p < 0.05$) in *Notch2*^{Q2319X} cultures. *Hes1* mRNA was increased as control and *Notch2*^{Q2319X} mutant cells matured, although the increase was more pronounced in *Notch2*^{Q2319X} cells, which were the only cultures expressing *Notch2* mutant transcripts (Fig. 6). *Hey1*, *-2,* and *-L* transcripts were not detected in either control or *Notch2*^{Q2319X} bone marrow mononuclear cell cultures (data not shown). To verify these results and to determine whether Notch activation was required for the effects observed, in a subsequent experiment bone marrow mononuclear cells were isolated and expanded in the presence of M-Csf at 100 ng/ml for 6 days followed by the addition of Rankl at 30 ng/ml in the presence of M-Csf at 30 ng/ml. The cultures were conducted in the absence and presence of the γ-secretase inhibitor LY450139 at 1 μM, to prevent activation of Notch and release of the NICD. Osteoclasts formed 5 days following cellular exposure to Rankl, and the number of osteoclasts was greater in *Notch2*^{Q2319X} cultures than in controls (Fig. 7). The γ-secretase inhibitor LY450139 decreased the formation of osteoclasts in the initial phases of osteoclast differentiation in control cultures, although not after 8 days of Rankl exposure. These findings confirm previous work suggesting that Notch activation is required for basal osteoclastogenesis (20). LY450139 precluded the effect of the *Notch2*^{Q2319X} mutation on osteoclastogenesis demonstrating that Notch activation is required for this effect of Notch2. *Notch2*^{Q2319X} osteoclasts expressed *Notch2* mutant transcripts, whereas control cells did not. There was an increase in the levels of *Hes1* mRNA, confirming activation of Notch signaling, and of *Acp5* (encoding for TRAP) mRNA in *Notch2*^{Q2319X} cells; LY450139 suppressed the expression of both genes in control and mutant cells (Fig. 7). Neither control nor *Notch2*^{Q2319X} mutant cells expressed detectable levels of *Hey1*, *-2,* or *-L* transcripts (data not shown). These results demonstrate that, in the context of the *Notch2*^{Q2319X} mutation, there is an increase in the pre-osteoclast cell pool as well as in its ability to differentiate into mature osteoclasts, and Notch activation is required for these effects.

To determine the effect of the *Notch2*^{Q2319X} mutation on bone resorption, bone marrow mononuclear cells from control and *Notch2*^{Q2319X} mutants were expanded in the presence of

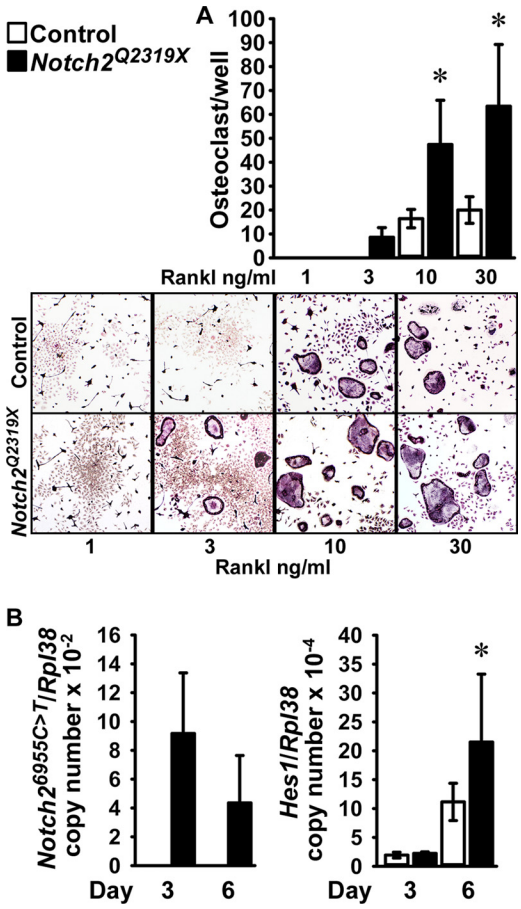

FIGURE 6. **Bone marrow mononuclear cells, harvested from femurs of *Notch2*^{Q2319X} mutant (*black bars*) and wild type littermate controls (*white bars*) were isolated by Ficoll-Hypaque gradient centrifugation and cultured for 6 days in the presence of M-Csf at 30 ng/ml and Rankl at 1–30 ng/ml.** *A,* cultures were assessed for TRAP by enzyme histochemistry. Values are means ± S.D.; $n = 6$ for all data sets. The *lower panel* shows representative culture fields of TRAP-stained multinucleated cells. *B,* cultures were assessed for *Notch2*$^{6955C\rightarrow T}$ (*Notch2*^{Q2319X}) and *Hes1* mRNA levels expressed as copy number corrected for *Rpl38*. Values are means ± S.D. Number of observations: $n = 4$ for control and *Notch2*^{Q2319X} at 3 and 6 days. *, significantly different between *Notch2*^{Q2319X} mutant and control cells, $p < 0.05$ by two-way analysis of variance with Holm-Sidak post hoc analysis.

M-Csf and seeded on bovine bone slices and cultured in the presence of M-Csf and Rankl. Sixteen days following the addition of Rankl, there was a greater number of pits and resorption area in the context of the *Notch2*^{Q2319X} mutation (Fig. 7). The effect was partially dependent on the activation of Notch because the number of pits, but not the resorption area, was significantly lower in *Notch2*^{Q2319X} cells in the presence of the γ-secretase inhibitor LY450139 (Fig. 7). An increase in bone resorption was observed in the presence of LY450139 alone. This may represent the inhibition of other signals targeted by γ-secretase because the inhibitor is not specific for Notch2 activation. It is possible that LY450139 inhibited Notch1 activation which, in contrast to Notch2, has been shown to decrease bone resorption (13).

Discussion

Our findings indicate that a global *Notch2*^{Q2319X} gain-of-function mutation causes osteopenia affecting both cancellous and cortical bone. The phenotype appeared as early as 1 month of age and was accompanied by a shortening of the femoral length suggesting a possible effect on endochondral bone formation and an influence by the *Notch2*^{Q2319X} mutation on skeletal development. The phenotype of 1-month-old mice harboring the *Notch2*^{Q2319X} mutation could be attributed to an increase in osteoclast number and bone resorption. It is of interest that there was a subsequent increase in osteoblast number and mineral apposition rate observed in 3-month-old male, but not female, mutant mice possibly representing a delayed compensatory response or increased bone remodeling. This response may explain a partial recovery in cancellous and cortical bone architecture. Although 1-month-old female mice also exhibited a cancellous bone osteopenic phenotype, it was less pronounced than in male mice, but as female mice matured the osteopenia became more evident. Biochemical markers of bone turnover were not affected in *Notch2*^{Q2319X} mutant mice, but this can be explained by limited sensitivity of the assays and variability of results (63, 64).

The phenotype of the *Notch2*^{Q2319X} mutant mouse recapitulates aspects of Hajdu Cheney syndrome, a progressive disorder characterized by a high degree of phenotypical pleiotropy. Some of the facial features of the syndrome appear in the first few months of life, but the clinical manifestations of the syndrome, including osteoporosis and acral osteolysis, are progressive and more evident during adolescence and adulthood (68, 69). It is of interest that *Notch2*^{Q2319X} mutant Hajdu Cheney mice did not exhibit detectable acral osteolysis or obvious neurological manifestations reported in humans affected by the disease. However, our work is limited to the study of young mice and additional phenotypic manifestations may appear in aging mice.

The phenotype observed in Hajdu Cheney *Notch2*^{Q2319X} mutant mice is distinct from the one reported following the activation of Notch1 in osteoblasts (7, 16). Notch1 activation in immature and mature osteoblasts leads to pronounced osteopenia due to an arrest of osteoblast maturation and function. Because the *Notch2*^{Q2319X} global mutation affects all cell lineages, an osteopenic phenotype secondary to a decrease in osteoblast number or function was conceivable. However, there was no evidence that Hajdu Cheney mutants had decreased osteoblast number or function in cancellous bone, and *in vitro* experiments revealed no changes in the expression of osteoblast gene markers in cultures of calvarial osteoblasts from *Notch2*^{Q2319X} mutants. Importantly, the phenotype of 1-month-old mice revealed a lack of a bone-forming response to enhanced bone resorption, possibly invoking a direct or indirect inhibition of this process under conditions of Notch2 activation. In this context, we have found that Notch2 induces Nfatc2 in skeletal cells, and Nfatc2 suppresses osteoblast differentiation and function and may contribute to the uncoupling of a bone-forming response to the increase in bone resorption (70, 71).[3] Histomorphometric analysis of cortical bone confirmed an increase in osteoclast number and bone resorption in the endocortical surface of 1-month-old *Notch2*^{Q2319X} mutants.

The osteopenic phenotype of the Hajdu Cheney *Notch2*^{Q2319X} mutant mouse can be explained by an increase in

[3] S. Zanotti and E. Canalis, unpublished observations.

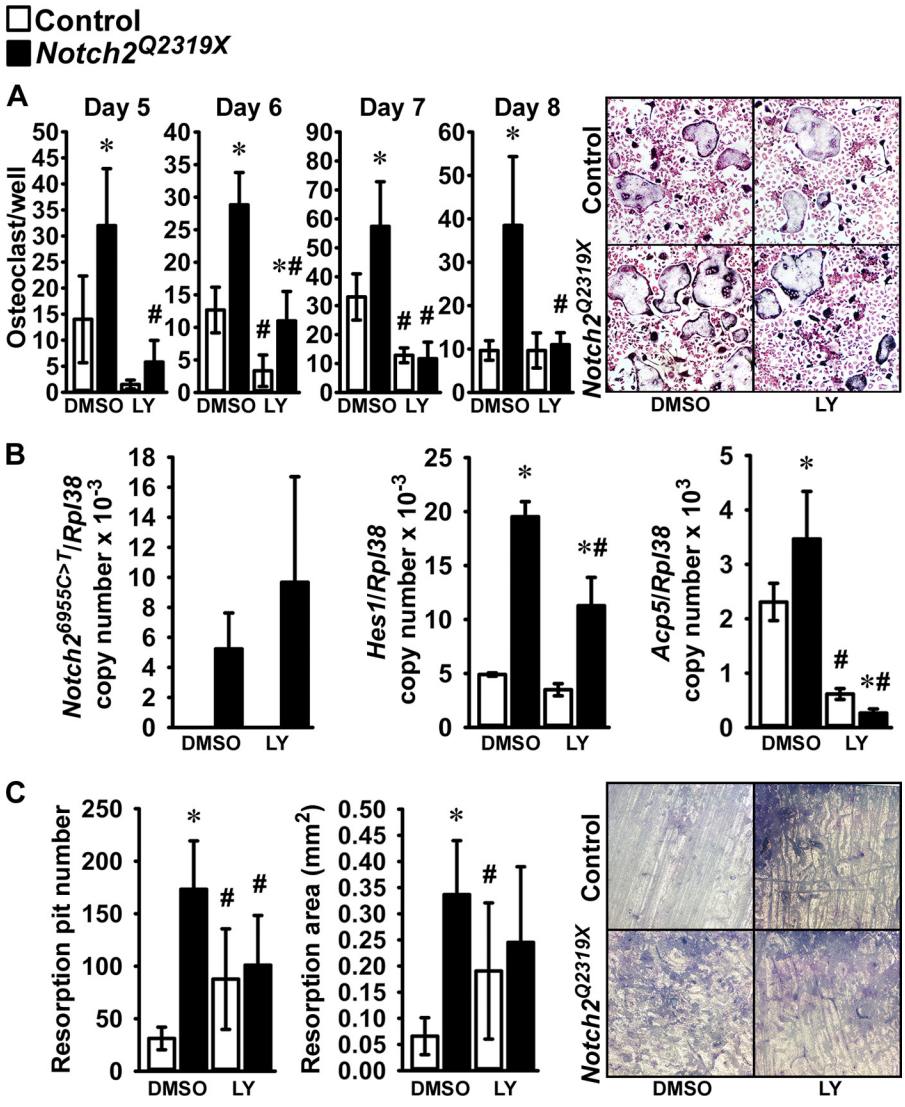

FIGURE 7. **Bone marrow mononuclear cells, harvested from femurs of *Notch2*^{Q2319X} mutant (*black bars*) and wild type littermate controls (*white bars*) were cultured in the presence of M-Csf at 100 ng/ml for 6 days and switched to 30 ng/ml M-Csf- and 30 ng/ml Rankl-containing medium.** Cultures were assessed in *A* for TRAP by enzyme histochemistry 5–8 days following exposure to Rankl. Values are means ± S.D.; $n = 6$ for all data sets except for *Notch2*^{Q2319X} DMSO at day 5 where $n = 5$; the *right upper panel* shows representative culture fields of TRAP-stained multinucleated cells 8 days after the addition of Rankl. *B,* cultures were assessed for *Notch2*$^{6955C\rightarrow T}$ (*Notch2*^{Q2319X}), *Hes1,* and *Acp5* mRNA expression 8 days following exposure to Rankl. Values are means ± S.D.; $n = 4$ for all data sets. *C,* cultures were assessed for bone resorption as determined by resorption pit number and area 16 days following exposure to Rankl. Values are means ± S.D.; $n = 6$ for all data sets in control and in *Notch2*^{Q2319X} in DMSO or LY450139 (*LY*). A representative culture showing resorption pits is presented in the *right lower panel*. Cultures were conducted in the presence of LY450139 at 1 μM or DMSO vehicle started at the time of Rankl addition and continued throughout the culture period. *, significantly different between *Notch2*^{Q2319X} mutant and control cells, $p < 0.05$. #, significantly different between LY450139 and DMSO, $p < 0.05$, both two-way analysis of variance with Holm-Sidak post hoc analysis.

bone resorption and osteoclastogenesis, an effect that has been reported selectively for Notch2 but not for Notch1 (13, 20). Notch2 enhances osteoclastogenesis by interacting with NF-κB on *Nfatc1* regulatory elements in cells of the osteoclast lineage (20). A recent study conducted in *Rbpjκ* null mice demonstrated that Rbpjκ inhibits osteoclastogenesis, an effect similar to that reported for Notch1 (72). This would suggest that canonical Notch signaling is responsible for the inhibitory effect of Notch1 on osteoclastogenesis because Rbpjκ is required for the activation of this signaling pathway. It may also suggest that the induction of osteoclastogenesis by Notch2 operates by non-canonical signaling pathways and that the direct interactions between the Notch2 intracellular domain and NF-κB on the *Nfatc1* promoter do not require activation of Notch canonical signaling. It is also possible that interactions between the Notch2 intracellular domain and Rbpjκ are distinct from those of Notch1, and they may result in different downstream events than those reported for Notch1 (73). It is of interest that Notch2, like Notch1, induced the expression of the canonical target genes *Hes1*, *Hey1, Hey2,* and *HeyL* in skeletal cells indicating a capacity to activate Notch canonical signaling. However, induction of Notch target genes may simply represent activation of Notch signaling and not necessarily imply that the canonical target genes are responsible for the effects observed. Although there was a non-preferential increase in canonical Notch target genes, *Hey1*, *Hey2,* and *HeyL* in *Notch2*^{Q2319X} mutant osteoblasts, this was not the case in cells of the osteoclast lineage that expressed *Hes1* but not *Hey1*,

Hey2, and *HeyL*. Confirming previous work, the induction of *Hes1* in osteoclasts was dependent not only on Notch2 activation but also on the degree of osteoclast maturation (20). Moreover, the phenotype observed in *Notch2*^{Q2319X} male mice is in accordance with the known effects of Hes1 on osteoclastogenesis and bone resorption (74). This may suggest that Hes1 is responsible for selected actions of Notch2 or of the *Notch2*^{Q2319X} mutants in the skeleton.

Although these studies demonstrate induction of Notch target gene mRNA and transactivation, both representing enhanced Notch activation by the *Notch2*^{Q2319X} mutation, we were not able to determine the mechanism responsible for the gain-of-function. Technical difficulties prevented us from determining Notch2 protein levels and demonstrating a more stable Notch2 protein product in *Notch2*^{Q2319X} mutant cells. This is because antibodies to detect cleaved Notch2 are not available (75). We suggest that stabilization of the truncated Notch2 protein is the cause of enhanced Notch2 signaling in mice. The mutation in the mouse, like in humans, was created upstream from the PEST domain, which is required for protein degradation (76). Moreover, mutations in the same region of exon 34 of either *Notch1* or *Notch2* are associated with Notch gain-of-function and signal activation (66, 78, 79). Another limitation of the studies presented is the use of a global knock-in *Notch2*^{Q2319X} mutation. Although the intent was to reproduce the human syndrome, we cannot exclude systemic effects of the mutant *Notch2*^{Q2319X} on the skeleton.

It is important to note that Notch operates by distinct mechanisms in different cellular compartments. In bone *Notch2*^{Q2319X} mutants expressed increased levels of Rankl without changes in osteoprotegerin expression so that the Rankl/osteoprotegerin ratio was increased at the mRNA level, possibly contributing to the resorptive phenotype observed. It is of interest that Rankl expression was increased in both osteoblasts and osteocytes of mutant mice, and this increase was dependent on Notch activation because it was not observed in osteocyte-rich cultures treated with a γ-secretase inhibitor. The increased number of osteoclasts and bone resorption may be secondary to a diversity of mechanisms in addition to the enhanced Rankl expression. The osteoclast cell precursor pool was increased in *Notch2*^{Q2319X} mutants by ~25%. Moreover, their capacity to differentiate into mature osteoclasts, capable of resorbing bone, in response to Rankl was enhanced, and these mechanisms serve to explain the increased osteoclast number and bone resorption in *Notch2*^{Q2319X} mutants. These results are consistent with the reported stimulatory effects of Notch2 on osteoclastogenesis and are congruent with a mutation causing a Notch2 gain-of-function.

There was no change in the number of osteocytes in either cancellous or cortical bone of *Notch2*^{Q2319X} mutants, and caspase 3 expression in osteocytes was not increased, suggesting that osteocyte apoptosis was not affected and probably not responsible for the increased cancellous and cortical bone resorption. Although osteocytes are a rich source of Rankl and osteocyte apoptosis precedes osteoclast recruitment during unloading, inhibition of osteocyte apoptosis prevents the increase in Rankl but does not stop bone resorption suggesting that additional mechanisms play a role in the regulation of bone resorption by these cells (77, 80–82). The cortical porosity observed is likely secondary to the increased osteoclastogenesis and bone resorption in *Notch2*^{Q2319X} mutants.

Although one needs to be cautious with the extrapolation of these results to human disease, an increase in bone resorption could explain the pronounced osteoporosis suffered by subjects with Hajdu Cheney syndrome. The osteolytic lesions observed in these patients reflect a localized resorptive event as well as an inflammatory process (68). If enhanced bone resorption is responsible for the disease, anti-resorptive therapy could prove beneficial to patients with Hajdu Cheney syndrome; however, clinical data on its effectiveness are sparse. Although enhanced bone resorption was observed, additional undiscovered mechanisms may contribute to the bone loss.

In conclusion, *Notch2*^{Q2319X} mutant mice replicating the mutation found in subjects with Hajdu Cheney syndrome exhibit marked osteopenia; enhanced osteoclastogenesis and bone resorption are in part responsible for the phenotype observed.

Author Contributions—E. C. designed the research studies, analyzed the data, and wrote the manuscript. L. S. conducted the experiments. S. P. Y, designed and created the mouse model. K. L. conducted the experiments. S. Z. acquired and analyzed the data, conducted the experiments, and edited the manuscript.

Acknowledgments—We thank J. Lian for Bglap cDNA, D. Srivastava for HeyL cDNA; A. Rao for Nfatc1 cDNA; R. Wu for Gapdh cDNA; L. J. Strobl for 12×CSL-Luc reporter construct; M. M. Maier for Hey1-Luc promoter construct; T. Iso for Hey2-Luc promoter construct and Hey1 and Hey2 cDNAs; Dr. Lorenzo for helpful advice and for providing bovine bone slices for resorption assays; Allison Kent and David Bridgewater for technical assistance; and Mary Yurczak for secretarial support.

References

1. Fortini, M. E. (2009) Notch signaling: the core pathway and its posttranslational regulation. *Dev. Cell* **16,** 633–647
2. Mumm, J. S., and Kopan, R. (2000) Notch signaling: from the outside in. *Dev. Biol.* **228,** 151–165
3. Sahlgren, C., and Lendahl, U. (2006) Notch signaling and its integration with other signaling mechanisms. *Regen. Med.* **1,** 195–205
4. Zanotti, S., and Canalis, E. (2010) Notch and the skeleton. *Mol. Cell. Biol.* **30,** 886–896
5. Engin, F., Yao, Z., Yang, T., Zhou, G., Bertin, T., Jiang, M. M., Chen, Y., Wang, L., Zheng, H., Sutton, R. E., Boyce, B. F., and Lee, B. (2008) Dimorphic effects of Notch signaling in bone homeostasis. *Nat. Med.* **14,** 299–305
6. Hilton, M. J., Tu, X., Wu, X., Bai, S., Zhao, H., Kobayashi, T., Kronenberg, H. M., Teitelbaum, S. L., Ross, F. P., Kopan, R., and Long, F. (2008) Notch signaling maintains bone marrow mesenchymal progenitors by suppressing osteoblast differentiation. *Nat. Med.* **14,** 306–314
7. Zanotti, S., Smerdel-Ramoya, A., Stadmeyer, L., Durant, D., Radtke, F., and Canalis, E. (2008) Notch inhibits osteoblast differentiation and causes osteopenia. *Endocrinology* **149,** 3890–3899
8. Zanotti, S., and Canalis, E. (2012) Notch regulation of bone development and remodeling and related skeletal disorders. *Calcif. Tissue Int.* **90,** 69–75
9. Kovall, R. A. (2008) More complicated than it looks: assembly of Notch pathway transcription complexes. *Oncogene* **27,** 5099–5109
10. Nam, Y., Sliz, P., Song, L., Aster, J. C., and Blacklow, S. C. (2006) Structural basis for cooperativity in recruitment of MAML coactivators to Notch

transcription complexes. *Cell* **124,** 973–983
11. Schroeter, E. H., Kisslinger, J. A., and Kopan, R. (1998) Notch-1 signalling requires ligand-induced proteolytic release of intracellular domain. *Nature* **393,** 382–386
12. Wilson, J. J., and Kovall, R. A. (2006) Crystal structure of the CSL-Notch-Mastermind ternary complex bound to DNA. *Cell* **124,** 985–996
13. Bai, S., Kopan, R., Zou, W., Hilton, M. J., Ong, C. T., Long, F., Ross, F. P., and Teitelbaum, S. L. (2008) NOTCH1 regulates osteoclastogenesis directly in osteoclast precursors and indirectly via osteoblast lineage cells. *J. Biol. Chem.* **283,** 6509–6518
14. Dallas, D. J., Genever, P. G., Patton, A. J., Millichip, M. I., McKie, N., and Skerry, T. M. (1999) Localization of ADAM10 and Notch receptors in bone. *Bone* **25,** 9–15
15. Pereira, R. M., Delany, A. M., Durant, D., and Canalis, E. (2002) Cortisol regulates the expression of Notch in osteoblasts. *J. Cell. Biochem.* **85,** 252–258
16. Canalis, E., Parker, K., Feng, J. Q., and Zanotti, S. (2013) Osteoblast lineage-specific effects of Notch activation in the skeleton. *Endocrinology* **154,** 623–634
17. Zanotti, S., Smerdel-Ramoya, A., and Canalis, E. (2011) Reciprocal regulation of notch and nuclear factor of activated T-cells (NFAT)c1 transactivation in osteoblasts. *J. Biol. Chem.* **286,** 4576–4588
18. Canalis, E., Adams, D. J., Boskey, A., Parker, K., Kranz, L., and Zanotti, S. (2013) Notch signaling in osteocytes differentially regulates cancellous and cortical bone remodeling. *J. Biol. Chem.* **288,** 25614–25625
19. Tu, X., Chen, J., Lim, J., Karner, C. M., Lee, S. Y., Heisig, J., Wiese, C., Surendran, K., Kopan, R., Gessler, M., and Long, F. (2012) Physiological notch signaling maintains bone homeostasis via RBPjk and Hey upstream of NFATc1. *PLoS Genet.* **8,** e1002577
20. Fukushima, H., Nakao, A., Okamoto, F., Shin, M., Kajiya, H., Sakano, S., Bigas, A., Jimi, E., and Okabe, K. (2008) The association of Notch2 and NF-κB accelerates RANKL-induced osteoclastogenesis. *Mol. Cell. Biol.* **28,** 6402–6412
21. Conlon, R. A., Reaume, A. G., and Rossant, J. (1995) Notch1 is required for the coordinate segmentation of somites. *Development* **121,** 1533–1545
22. Swiatek, P. J., Lindsell, C. E., del Amo, F. F., Weinmaster, G., and Gridley, T. (1994) Notch1 is essential for postimplantation development in mice. *Genes Dev.* **8,** 707–719
23. Weinmaster, G., Roberts, V. J., and Lemke, G. (1992) Notch2: a second mammalian Notch gene. *Development* **116,** 931–941
24. Bigas, A., Martin, D. I., and Milner, L. A. (1998) Notch1 and Notch2 inhibit myeloid differentiation in response to different cytokines. *Mol. Cell. Biol.* **18,** 2324–2333
25. Cheney, W. D. (1965) Acro-Osteolysis. *Am. J. Roentgenol. Radium. Ther. Nucl. Med.* **94,** 595–607
26. Hajdu, N., and Kauntze, R. (1948) Cranio-skeletal dysplasia. *Br. J. Radiol.* **21,** 42–48
27. Gray, M. J., Kim, C. A., Bertola, D. R., Arantes, P. R., Stewart, H., Simpson, M. A., Irving, M. D., and Robertson, S. P. (2012) Serpentine fibula polycystic kidney syndrome is part of the phenotypic spectrum of Hajdu-Cheney syndrome. *Eur. J. Hum. Genet.* **20,** 122–124
28. Isidor, B., Lindenbaum, P., Pichon, O., Bézieau, S., Dina, C., Jacquemont, S., Martin-Coignard, D., Thauvin-Robinet, C., Le Merrer, M., Mandel, J. L., David, A., Faivre, L., Cormier-Daire, V., Redon, R., and Le Caignec, C. (2011) Truncating mutations in the last exon of NOTCH2 cause a rare skeletal disorder with osteoporosis. *Nat. Genet.* **43,** 306–308
29. Majewski, J., Schwartzentruber, J. A., Caqueret, A., Patry, L., Marcadier, J., Fryns, J. P., Boycott, K. M., Ste-Marie, L. G., McKiernan, F. E., Marik, I., Van Esch, H., FORGE Canada Consortium, Michaud, J. L., and Samuels, M. E. (2011) Mutations in NOTCH2 in families with Hajdu-Cheney syndrome. *Hum. Mutat.* **32,** 1114–1117
30. Simpson, M. A., Irving, M. D., Asilmaz, E., Gray, M. J., Dafou, D., Elmslie, F. V., Mansour, S., Holder, S. E., Brain, C. E., Burton, B. K., Kim, K. H., Pauli, R. M., Aftimos, S., Stewart, H., Kim, C. A., *et al.* (2011) Mutations in NOTCH2 cause Hajdu-Cheney syndrome, a disorder of severe and progressive bone loss. *Nat. Genet.* **43,** 303–305
31. Zhao, W., Petit, E., Gafni, R. I., Collins, M. T., Robey, P. G., Seton, M., Miller, K. K., and Mannstadt, M. (2013) Mutations in NOTCH2 in patients with Hajdu-Cheney syndrome. *Osteoporos. Int.* **24,** 2275–2281
32. Udell, J., Schumacher, H. R., Jr., Kaplan, F., and Fallon, M. D. (1986) Idiopathic familial acroosteolysis: histomorphometric study of bone and literature review of the Hajdu-Cheney syndrome. *Arthritis Rheum.* **29,** 1032–1038
33. Blumenauer, B. T., Cranney, A. B., and Goldstein, R. (2002) Acro-osteolysis and osteoporosis as manifestations of the Hajdu-Cheney syndrome. *Clin. Exp. Rheumatol.* **20,** 574–575
34. Brown, D. M., Bradford, D. S., Gorlin, R. J., Desnick, R. J., Langer, L. O., Jowsey, J., and Sauk, J. J. (1976) The acro-osteolysis syndrome: morphologic and biochemical studies. *J. Pediatr.* **88,** 573–580
35. Avela, K., Valanne, L., Helenius, I., and Makitie, O. (2011) Hajdu-Cheney syndrome with severe dural ectasia. *Am. J. Med. Genet.* **155,** 595–598
36. Tang, S. H., Silva, F. J., Tsark, W. M., and Mann, J. R. (2002) A Cre/loxP-deleter transgenic line in mouse strain 129S1/SvImJ. *Genesis* **32,** 199–202
37. Bouxsein, M. L., Boyd, S. K., Christiansen, B. A., Guldberg, R. E., Jepsen, K. J., and Müller, R. (2010) Guidelines for assessment of bone microstructure in rodents using micro-computed tomography. *J. Bone Miner. Res.* **25,** 1468–1486
38. Glatt, V., Canalis, E., Stadmeyer, L., and Bouxsein, M. L. (2007) Age-related changes in trabecular architecture differ in female and male C57BL/6J mice. *J. Bone Miner. Res.* **22,** 1197–1207
39. Dempster, D. W., Compston, J. E., Drezner, M. K., Glorieux, F. H., Kanis, J. A., Malluche, H., Meunier, P. J., Ott, S. M., Recker, R. R., and Parfitt, A. M. (2013) Standardized nomenclature, symbols, and units for bone histomorphometry: a 2012 update of the report of the ASBMR Histomorphometry Nomenclature Committee. *J. Bone Miner. Res.* **28,** 2–17
40. Parfitt, A. M., Drezner, M. K., Glorieux, F. H., Kanis, J. A., Malluche, H., Meunier, P. J., Ott, S. M., and Recker, R. R. (1987) Bone histomorphometry: standardization of nomenclature, symbols, and units. Report of the ASBMR Histomorphometry Nomenclature Committee. *J. Bone Miner. Res.* **2,** 595–610
41. Hefley, T., Cushing, J., and Brand, J. S. (1981) Enzymatic isolation of cells from bone: cytotoxic enzymes of bacterial collagenase. *Am. J. Physiol.* **240,** C234–C238
42. Zanotti, S., Kalajzic, I., Aguila, H. L., and Canalis, E. (2014) Sex and genetic factors determine osteoblastic differentiation potential of murine bone marrow stromal cells. *PLoS ONE* **9,** e86757
43. Strobl, L. J., Höfelmayr, H., Stein, C., Marschall, G., Brielmeier, M., Laux, G., Bornkamm, G. W., and Zimber-Strobl, U. (1997) Both Epstein-Barr viral nuclear antigen 2 (EBNA2) and activated Notch1 transactivate genes by interacting with the cellular protein RBP-Jκ. *Immunobiology* **198,** 299–306
44. Maier, M. M., and Gessler, M. (2000) Comparative analysis of the human and mouse Hey1 promoter: Hey genes are new Notch target genes. *Biochem. Biophys. Res. Commun.* **275,** 652–660
45. Iso, T., Chung, G., Hamamori, Y., and Kedes, L. (2002) HERP1 is a cell type-specific primary target of Notch. *J. Biol. Chem.* **277,** 6598–6607
46. Halleux, C., Kramer, I., Allard, C., and Kneissel, M. (2012) Isolation of mouse osteocytes using cell fractionation for gene expression analysis. *Methods Mol. Biol.* **816,** 55–66
47. Borgegard, T., Juréus, A., Olsson, F., Rosqvist, S., Sabirsh, A., Rotticci, D., Paulsen, K., Klintenberg, R., Yan, H., Waldman, M., Stromberg, K., Nord, J., Johansson, J., Regner, A., Parpal, S., *et al.* (2012) First and second generation γ-secretase modulators (GSMs) modulate amyloid-β (Aβ) peptide production through different mechanisms. *J. Biol. Chem.* **287,** 11810–11819
48. Mun, S. H., Oh, D., and Lee, S. K. (2014) Macrophage migration inhibitory factor down-regulates the RANKL-RANK signaling pathway by activating Lyn tyrosine kinase in mouse models. *Arthritis Rheumatol.* **66,** 2482–2493
49. Mun, S. H., Won, H. Y., Hernandez, P., Aguila, H. L., and Lee, S. K. (2013) Deletion of CD74, a putative MIF receptor, in mice enhances osteoclastogenesis and decreases bone mass. *J. Bone Miner. Res.* **28,** 948–959
50. Jacome-Galarza, C. E., Lee, S. K., Lorenzo, J. A., and Aguila, H. L. (2011) Parathyroid hormone regulates the distribution and osteoclastogenic potential of hematopoietic progenitors in the bone marrow. *J. Bone Miner. Res.* **26,** 1207–1216
51. Aguila, H. L., Mun, S. H., Kalinowski, J., Adams, D. J., Lorenzo, J. A., and

Lee, S. K. (2012) Osteoblast-specific overexpression of human interleukin-7 rescues the bone mass phenotype of interleukin-7-deficient female mice. *J. Bone Miner. Res.* **27,** 1030–1042
52. Nazarenko, I., Pires, R., Lowe, B., Obaidy, M., and Rashtchian, A. (2002) Effect of primary and secondary structure of oligodeoxyribonucleotides on the fluorescent properties of conjugated dyes. *Nucleic Acids Res.* **30,** 2089–2195
53. Nazarenko, I., Lowe, B., Darfler, M., Ikonomi, P., Schuster, D., and Rashtchian, A. (2002) Multiplex quantitative PCR using self-quenched primers labeled with a single fluorophore. *Nucleic Acids Res.* **30,** e37
54. Lian, J., Stewart, C., Puchacz, E., Mackowiak, S., Shalhoub, V., Collart, D., Zambetti, G., and Stein, G. (1989) Structure of the rat osteocalcin gene and regulation of vitamin D-dependent expression. *Proc. Natl. Acad. Sci. U.S.A.* **86,** 1143–1147
55. Iso, T., Sartorelli, V., Chung, G., Shichinohe, T., Kedes, L., and Hamamori, Y. (2001) HERP, a new primary target of Notch regulated by ligand binding. *Mol. Cell. Biol.* **21,** 6071–6079
56. Nakagawa, O., Nakagawa, M., Richardson, J. A., Olson, E. N., and Srivastava, D. (1999) HRT1, HRT2, and HRT3: a new subclass of bHLH transcription factors marking specific cardiac, somitic, and pharyngeal arch segments. *Dev. Biol.* **216,** 72–84
57. Glinka, A., Wu, W., Delius, H., Monaghan, A. P., Blumenstock, C., and Niehrs, C. (1998) Dickkopf-1 is a member of a new family of secreted proteins and functions in head induction. *Nature* **391,** 357–362
58. Monticelli, S., and Rao, A. (2002) NFAT1 and NFAT2 are positive regulators of IL-4 gene transcription. *Eur. J. Immunol.* **32,** 2971–2978
59. Kutyavin, I. V., Afonina, I. A., Mills, A., Gorn, V. V., Lukhtanov, E. A., Belousov, E. S., Singer, M. J., Walburger, D. K., Lokhov, S. G., Gall, A. A., Dempcy, R., Reed, M. W., Meyer, R. B., and Hedgpeth, J. (2000) 3′-minor groove binder-DNA probes increase sequence specificity at PCR extension temperatures. *Nucleic Acids Res.* **28,** 655–661
60. Gibson, D. G., Young, L., Chuang, R. Y., Venter, J. C., Hutchison, C. A., 3rd, and Smith, H. O. (2009) Enzymatic assembly of DNA molecules up to several hundred kilobases. *Nat. Methods* **6,** 343–345
61. Kouadjo, K. E., Nishida, Y., Cadrin-Girard, J. F., Yoshioka, M., and St-Amand, J. (2007) Housekeeping and tissue-specific genes in mouse tissues. *BMC. Genomics* **8,** 127
62. Tso, J. Y., Sun, X. H., Kao, T. H., Reece, K. S., and Wu, R. (1985) Isolation and characterization of rat and human glyceraldehyde-3-phosphate dehydrogenase cDNAs: genomic complexity and molecular evolution of the gene. *Nucleic Acids Res.* **13,** 2485–2502
63. Herrmann, M. (2011) in *Osteoporosis Research- Animal Models* (Duque, G., Watanabe, K., ed) pp. 57–82, Springer, New York
64. Seibel, M. J. (2005) Biochemical markers of bone turnover: part I: biochemistry and variability. *Clin. Biochem. Rev.* **26,** 97–122
65. Kiel, M. J., Velusamy, T., Betz, B. L., Zhao, L., Weigelin, H. G., Chiang, M. Y., Huebner-Chan, D. R., Bailey, N. G., Yang, D. T., Bhagat, G., Miranda, R. N., Bahler, D. W., Medeiros, L. J., Lim, M. S., and Elenitoba-Johnson, K. S. (2012) Whole-genome sequencing identifies recurrent somatic NOTCH2 mutations in splenic marginal zone lymphoma. *J. Exp. Med.* **209,** 1553–1565
66. Rossi, D., Trifonov, V., Fangazio, M., Bruscaggin, A., Rasi, S., Spina, V., Monti, S., Vaisitti, T., Arruga, F., Famà, R., Ciardullo, C., Greco, M., Cresta, S., Piranda, D., Holmes, A., *et al.* (2012) The coding genome of splenic marginal zone lymphoma: activation of NOTCH2 and other pathways regulating marginal zone development. *J. Exp. Med.* **209,** 1537–1551
67. Zhang, X., Shi, Y., Weng, Y., Lai, Q., Luo, T., Zhao, J., Ren, G., Li, W., Pan, H., Ke, Y., Zhang, W., He, Q., Wang, Q., and Zhou, R. (2014) The truncate mutation of Notch2 enhances cell proliferation through activating the NF-κB signal pathway in the diffuse large B-cell lymphomas. *PLoS ONE* **9,** e108747
68. Canalis, E., and Zanotti, S. (2014) Hajdu-Cheney syndrome: a review. *Orphanet J. Rare Dis.* **9,** 200
69. Descartes, M., Rojnueangnit, K., Cole, L., Sutton, A., Morgan, S. L., Patry, L., and Samuels, M. E. (2014) Hajdu-Cheney syndrome: phenotypical progression with *de novo* NOTCH2 mutation. *Clin. Dysmorphol.* **23,** 88–94
70. Zanotti, S., and Canalis, E. (2015) Activation of Nfatc2 in osteoblasts causes osteopenia. *J. Cell. Physiol.* **230,** 1689–1695
71. Zanotti, S., Smerdel-Ramoya, A., and Canalis, E. (2013) Nuclear factor of activated T-cells (Nfat)c2 inhibits Notch signaling in osteoblasts. *J. Biol. Chem.* **288,** 624–632
72. Li, S., Miller, C. H., Giannopoulou, E., Hu, X., Ivashkiv, L. B., and Zhao, B. (2014) RBP-J imposes a requirement for ITAM-mediated costimulation of osteoclastogenesis. *J. Clin. Invest.* **124,** 5057–5073
73. Yuan, Z., Friedmann, D. R., VanderWielen, B. D., Collins, K. J., and Kovall, R. A. (2012) Characterization of CSL (CBF-1, Su(H), Lag-1) mutants reveals differences in signaling mediated by Notch1 and Notch2. *J. Biol. Chem.* **287,** 34904–34916
74. Zanotti, S., Smerdel-Ramoya, A., and Canalis, E. (2011) Hairy and enhancer of split (HES)1 is a determinant of bone mass. *J. Biol. Chem.* **286,** 2648–2657
75. Habets, R. A., Groot, A. J., Yahyanejad, S., Tiyanont, K., Blacklow, S. C., and Vooijs, M. (2015) Human NOTCH2 is resistant to ligand-independent activation by metalloprotease Adam17. *J. Biol. Chem.* **290,** 14705–14716
76. Rogers, S., Wells, R., and Rechsteiner, M. (1986) Amino acid sequences common to rapidly degraded proteins: the PEST hypothesis. *Science* **234,** 364–368
77. Xiong, J., Onal, M., Jilka, R. L., Weinstein, R. S., Manolagas, S. C., and O'Brien, C. A. (2011) Matrix-embedded cells control osteoclast formation. *Nat. Med.* **17,** 1235–1241
78. Weng, A. P., Ferrando, A. A., Lee, W., Morris, J. P., 4th, Silverman, L. B., Sanchez-Irizarry, C., Blacklow, S. C., Look, A. T., and Aster, J. C. (2004) Activating mutations of NOTCH1 in human T cell acute lymphoblastic leukemia. *Science* **306,** 269–271
79. Breit, S., Stanulla, M., Flohr, T., Schrappe, M., Ludwig, W. D., Tolle, G., Happich, M., Muckenthaler, M. U., and Kulozik, A. E. (2006) Activating NOTCH1 mutations predict favorable early treatment response and long-term outcome in childhood precursor T-cell lymphoblastic leukemia. *Blood* **108,** 1151–1157
80. Aguirre, J. I., Plotkin, L. I., Stewart, S. A., Weinstein, R. S., Parfitt, A. M., Manolagas, S. C., and Bellido, T. (2006) Osteocyte apoptosis is induced by weightlessness in mice and precedes osteoclast recruitment and bone loss. *J. Bone Miner. Res.* **21,** 605–615
81. Nakashima, T., Hayashi, M., Fukunaga, T., Kurata, K., Oh-Hora, M., Feng, J. Q., Bonewald, L. F., Kodama, T., Wutz, A., Wagner, E. F., Penninger, J. M., and Takayanagi, H. (2011) Evidence for osteocyte regulation of bone homeostasis through RANKL expression. *Nat. Med.* **17,** 1231–1234
82. Plotkin, L. I., Gortazar, A. R., Davis, H. M., Condon, K. W., Gabilondo, H., Maycas, M., Allen, M. R., and Bellido, T. (2015) Inhibition of osteocyte apoptosis prevents the increase in osteocytic receptor activator of nuclear factor-κB ligand (RANKL) but does not stop bone resorption or the loss of bone induced by unloading. *J. Biol. Chem.* **290,** 18934–18942